


# Characterization of a phase plate for the creation of an optical homogeneous 2D trapping potential

**Student Paper****Author(s):**

Montalti, Nicolò 

**Publication date:**

2023

**Permanent link:**

<https://doi.org/10.3929/ethz-b-000638134>

**Rights / license:**

[In Copyright - Non-Commercial Use Permitted](#)



Eidgenössische Technische Hochschule Zürich  
Swiss Federal Institute of Technology Zurich

# Characterization of a phase plate for the creation of an optical homogeneous 2D trapping potential

Semester Project

Nicolò Montalti  
nmontalti@student.ethz.ch

Quantum Optics Group  
Departement of Physics, D-PHYS  
ETH Zürich

**Supervisor:**  
Prof. Tilman Esslinger

**Advisors:**  
Dr. Meng-Zi Huang  
Mohsen Talebi

October 18, 2023

## Abstract

In this report we investigate the possibility of using a custom-made phase plate to generate a flat potential for the creation of a 2D channel between two reservoirs in a quantum gas transport experiment. We first present a brief introduction to transport experiments with quantum gases together with a discussion on the dipole force and a review on spatial light modulation with phase plates. Then, we characterize the custom-made phase plate, with a particular focus on evaluating the flatness of the potential for different incoming beam sizes. The best results have been found for beam diameters close to 5 mm, although the specifications required a 6 mm beam. Some smaller findings include the development of a procedure to find the focal point and to align the phase plate to the beam. Finally, we discuss the potential implications of the inhomogeneity of the optical potential on the actual transport experiments.

# Contents

<b>Abstract</b>	<b>i</b>
<b>1 Introduction</b>	<b>1</b>
1.1 Analog and digital quantum simulation . . . . .	2
1.2 Transport experiments . . . . .	2
1.3 Outline . . . . .	3
<b>2 Theoretical background</b>	<b>5</b>
2.1 Atom-light interaction . . . . .	5
2.1.1 The dipole force . . . . .	5
2.2 Spatial light modulation . . . . .	7
2.2.1 Fourier optics . . . . .	7
2.2.2 Spatial light modulators: the phase plate . . . . .	9
2.2.3 Required specifications . . . . .	10
<b>3 Characterization of the phase plate</b>	<b>14</b>
3.1 Building the experimental setup . . . . .	14
3.1.1 Imaging system . . . . .	14
3.1.2 Test with the $0 - \pi$ phase plate . . . . .	16
3.1.3 Shaping the input beam . . . . .	17
3.2 Characterization . . . . .	21
3.2.1 Methods . . . . .	21
3.2.2 Results . . . . .	25
3.2.3 Additional considerations . . . . .	30
<b>4 Conclusions</b>	<b>36</b>
<b>Acknowledgements</b>	<b>37</b>

# Chapter 1

## Introduction

*“Nature isn’t classical, dammit, and if you want to make a simulation of nature, you’d better make it quantum mechanical, and by golly it’s a wonderful problem, because it doesn’t look so easy”*

— Richard Feynman

Predicting the behaviour of complex systems has always been an important goal of scientific research. From predicting the motion of stars and planets in our solar system, to understanding the behaviour of systems showing chaotic behaviours. In history, before scientists were able to find analytical solutions to many problems, they often relied on simulations. A celebrated example are the astronomical clocks that were built in Asia and Europe in the period between 1000 and 1500, such as the famous astronomical clock in Prague (1410) or the Zytglogge in Bern (1530). These complex machines were used to predict the position of astronomical objects such planets and constellations, and the phases and eclipses of the moon [1]. With the advent of quantum mechanics, a new kind of problems for which no analytical solution is possible was found. Given the high dimensionality of the Hilbert space of quantum many-body systems, classical computers cannot be used to find numerical solutions to this kind of problems. For example, simulating a system of  $N = 36$  qubit using two double-precision floating-point numbers to store a complex number, would require approximately  $2^{N+1} \times 8$  byte = 1 Terabyte of memory. For every additional qubit, this number would double. Richard Feynman was the first to propose to use a quantum system to handle this complexity, making use of the law of quantum mechanics itself. In 1982, he proposed to make use of one controllable quantum system simulate another [2]. In this way, a system of  $N$  quantum particles with two states could be simulated using another system of  $N$  qubits. The problem is then shifted to finding a system that can be easily tuned and controlled, such that it can be used to simulate a wide range of problems.

## 1.1 Analog and digital quantum simulation

To tackle this kind of problems, two different approaches have arisen in the past years: (digital) quantum computation and (analog) quantum simulation. In the first case, the information is encoded in qubits that can be found in two computational states  $|0\rangle$  and  $|1\rangle$ . In the latter, a direct mapping between the original problem (i.e. its Hamiltonian) and the simulating system is realized. Among the most promising platforms for quantum computation, we cite the use of superconducting circuits [3], Rydberg atoms [4] and trapped ions [5]. Whereas for quantum simulation, the use of ultracold quantum gases has gained increasing popularity [1].

For example, one of the first systems to be simulated with this platform was a system of electrons moving in an ionic periodic lattice potential. The electrons can be simulated using a gas of fermionic atoms trapped in an optical lattice potential. Here, the periodic potential through which the particles move is generated externally by making use of the interference pattern of overlapping laser beams [6]. It is performing an experiment of this kind that Bloch oscillations, predicted in 1929 by Felix Bloch [7], were directly observed in 1996 in a cloud of ultracold Caesium atoms [8], after being observed in 1992 through the emission of THz radiation by the electrons only in a semiconductor super lattice [9]. In this case, ultracold gases allowed the first direct observation of a phenomenon that was experimentally inaccessible for a solid state system, proving the potential of this technology. In the following years, new interesting experiments were proposed to simulate the behaviour of different quantum systems. Among them, we cite the use of optical lattices to investigate insulating and superfluid quantum phases [10], the use of cavities to mediate long range interactions [11] and the observation of quantized conductance in neutral matter [12]. In this report, we will focus on the latter, since the project was closely related to it.

## 1.2 Transport experiments

Transport experiments study the transport properties of particles moving from one reservoir to another. With an experiment of this kind, Krinner *et al.* were able to observe quantized conductance in the transport of neutral atoms driven by a chemical potential bias [12]. Their experiment let them investigate quantum conductors (systems for which conductance is quantized) with wide control over the channel geometry and the reservoir properties, such as interaction strength, size and thermalization rate. The basic setup of the experiment is shown in Fig. 1.1. A cloud of atoms is radially trapped with a dipole trap realized with a red-detuned laser. Along the  $y$  axis the confinement is produced by the magnetic field curvature of the Feshbach coils. This defines a cigar-shaped cloud elongated in the  $y$  direction. The cloud is then split in two reservoirs connected by a quasi-2D channel (e.g. due to a blue-detuned TEM<sub>01</sub> laser mode in the  $x$  direction). The blue-detuned laser creates a repulsive potential that confines the atoms in a quasi-2D region. The experiment is then carried on by creating a chemical potential imbalance between the two reservoirs and studying the conduction of atoms between them. Instead of acting on the chemical potential, different experiments can be realized by creating a temperature or a spin imbalance between the reservoirs.

The focus of this thesis is on the blue-detuned laser generating the 2D channel. In the

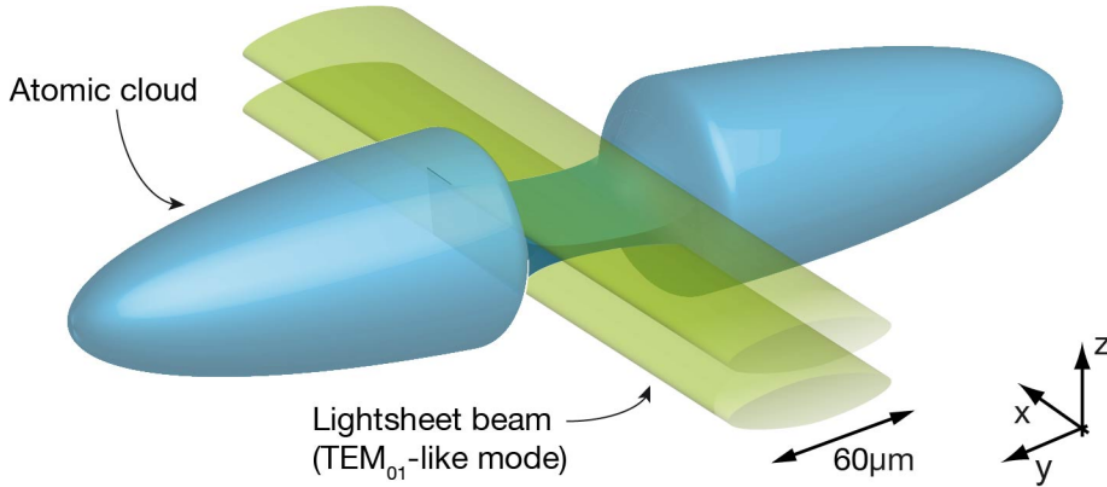


**Figure 1.1:** *Experimental setup. A cloud of atoms is trapped in a cigar-shaped potential. A blue-detuned  $TEM_{01}$  laser mode propagating in the  $x$  direction defined a quasi-2D channel connecting two smoothly connected reservoirs. Figure from Krinner [13].*

current experiment, the laser is in a  $TEM_{01}$  mode. The beam is shaped through a series of optical components shown in Fig. 1.2. It is clear that the potential inside the channel region is not uniform along the  $y$  direction. The conductance is influenced by this varying potential, and it would be desirable to have a uniform region connecting the two reservoir. The opportunity to create such a uniform 2D channel was previously investigated by Moritz Schmidt in his semester project [14]. Schmidt considered two options for generating a uniform light sheet: the use of liquid-crystal spatial light modulators and of custom-made  $0 - \pi$ , top-hat phase-plates. It was found that this second option is more suitable to the experiment, being at the same time able to satisfy the experimental requirements and considerably cheaper.

### 1.3 Outline

In this report, we analyse and characterize the custom-made phase plate ordered for the creation of the uniform light sheet. The phase plate had already been ordered based on Schmidt’s work, but it still had to be tested. In fact, despite knowing its expected behaviour, it was important to check the result that it produced in reality, finding the optimal configuration to make it work. In the next chapter, we will start reviewing the theory behind atom-light interaction and spatial light modulation. We will offer a brief overview on how atoms interact with light, and how this interaction can be exploited to generate an optical potential. Then, we will discuss how light can be shaped to generate an arbitrary intensity distribution, and therefore an arbitrary potential. To do so, we will review the basics of Fourier optics and the theory behind how phase plates work. Then, we will present the characterization of the phase plate that we received. We will discuss the experimental setup and the methods used to characterize it, especially focusing on the quantities we defined to quantify the “goodness”

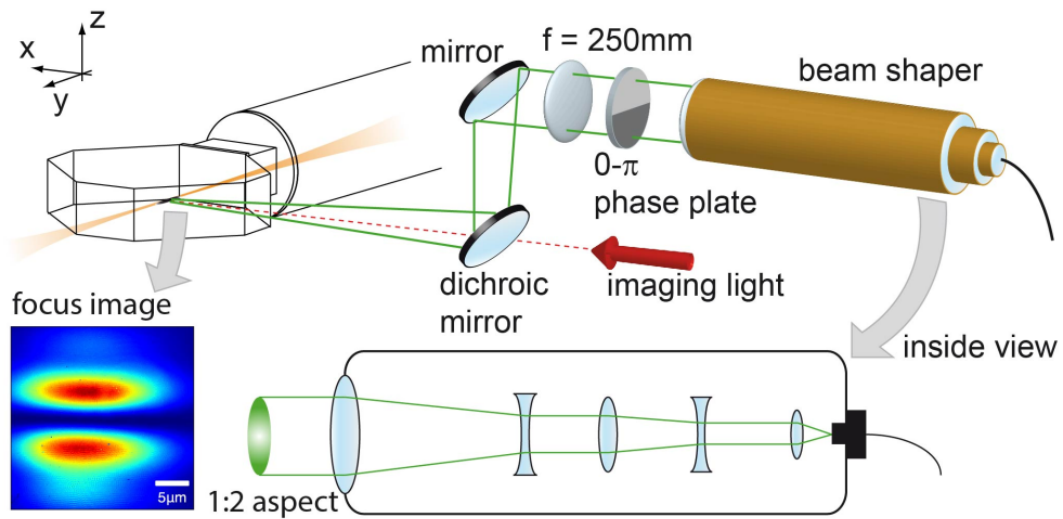


**Figure 1.2:** Generation of the  $TEM_{01}$  mode for the creation of 2D channel. A set of spherical and cylindrical lenses is used to expand the beam in the  $z$  direction. The beam is then sent to a  $0-\pi$  phase plate and focused through a 250 mm lens on the atomic cloud. Figure from Krinner [13].

of our results. Finally, we will discuss the results highlighting the most important aspects of using the phase plate optimally.



## Chapter 2

# Theoretical background

In this chapter we focus on how we can generate an arbitrary potential for a cloud of ultracold atoms. To understand it, we first need to review the basics of quantum optics that explain how atoms and light interact. We will see that this interaction creates a dipole force that can be used to trap the atoms. We will then focus on the theory of spatial light modulation. For it, we will present a discussion on Fourier optics and use it to understand how a phase plate can be used for such a purpose.

### 2.1 Atom-light interaction

At the quantum level, the interaction is usually interpreted as the absorption or emission of photons by the atoms. Despite this picture being accurate, matter can also interact with light through virtual absorption or emission processes, which have interesting behaviours. For this to happen, the frequency of light must be far detuned from the excitation energy of the atoms. An important effect of this type of interaction is the dipole force exerted by light on atoms. To understand the origin of this force, it is sufficient to remember that photons, besides energy, also carry momentum. When a photon is scattered by an atom, its momentum is transferred, generating an effective force that acts on the latter.

#### 2.1.1 The dipole force

To study this force in more detail, we present a discussion adapted from Jonathan Home's lecture notes on quantum optics. Following the standard approach in quantum optics, we model the atom as a two level system, where the energy levels are separated by an energy  $\hbar\omega_{eg}$ . We also consider light made of a single mode of frequency  $\omega/2\pi$ , like the light emitted by a laser. We start by writing the interaction Hamiltonian in the dipole approximation

$$H_{\text{int}} = -\mathbf{d} \cdot \mathbf{E}(\mathbf{r}) \quad (2.1)$$

where  $\mathbf{d}$  is the dipole moment operator,  $\mathbf{E}$  the electric field and  $\mathbf{r}$  the position of the atom. The Hamiltonian of the atom without the interaction term is

$$H_0 = \frac{\hbar\omega_{eg}}{2}\sigma_z + \frac{\mathbf{p}^2}{2m} \quad (2.2)$$

where  $\sigma_z$  is the third Pauli matrix,  $\mathbf{p}$  is the momentum operator and  $m$  the mass of the atom. Furthermore, we consider a classical electric field

$$\mathbf{E} = \frac{1}{2}E_0 f(\mathbf{r}) \left( e^{i(\mathbf{k}\cdot\mathbf{r}-\omega t)} + e^{-i(\mathbf{k}\cdot\mathbf{r}-\omega t)} \right) \boldsymbol{\epsilon} \quad (2.3)$$

where  $E_0$ ,  $\omega$  and  $\boldsymbol{\epsilon}$  are respectively the field strength, frequency and polarization. The function  $f(\mathbf{r})$  allows the field amplitude to vary spatially. Inserting Eq. (2.3) in Eq. (2.1), the interaction Hamiltonian can be rewritten as

$$H_{\text{int}} = -(\boldsymbol{\mu}_{eg} \cdot \hat{\boldsymbol{\epsilon}} E_0) \frac{f(\mathbf{r})}{2} (\sigma_+ + \sigma_-) \left( e^{i(\mathbf{k}\cdot\mathbf{r}-\omega t)} + e^{-i(\mathbf{k}\cdot\mathbf{r}-\omega t)} \right) \quad (2.4)$$

where  $\boldsymbol{\mu}_{eg} = \langle e | \mathbf{d} | g \rangle$ . It is now useful to move to the rotating frame with respect to the laser frequency. After transforming the Hamiltonian and performing the rotating wave approximation, we are left with

$$H = -\frac{\hbar\delta}{2}\omega_z + \frac{\mathbf{p}^2}{2m} + \frac{\hbar\Omega(\mathbf{r})}{2} \left( \sigma_+ e^{i\mathbf{k}\cdot\mathbf{r}} + \sigma_- e^{-i\mathbf{k}\cdot\mathbf{r}} \right) \quad (2.5)$$

with  $\Omega(\mathbf{r}) = \boldsymbol{\mu}_{eg} \cdot \hat{\boldsymbol{\epsilon}} E_0 f(\mathbf{r}) / \hbar$  and  $\delta = \omega - \omega_{eg}$ . We can find the resulting force applied on the atom by using Heisenberg's equation of motion

$$\begin{aligned} \mathbf{F} &= \frac{d\mathbf{p}}{dt} = \frac{i}{\hbar} [H, \mathbf{p}] \\ &= -\frac{\hbar}{2} \nabla \Omega(\mathbf{r}) \left( \sigma_+ e^{i\mathbf{k}\cdot\mathbf{r}} + \sigma_- e^{-i\mathbf{k}\cdot\mathbf{r}} \right) - \frac{\hbar}{2} \Omega(\mathbf{r}) i\mathbf{k} \left( \sigma_+ e^{i\mathbf{k}\cdot\mathbf{r}} - \sigma_- e^{-i\mathbf{k}\cdot\mathbf{r}} \right) \end{aligned} \quad (2.6)$$

We observe that we get two terms. The first, proportional to the spatial derivative of the field strength, includes a contribution in phase with the light field. It is the term that results in the dipole force exerted by the field on the atom, the one we are interested in. The second term is proportional to the field strength, and it has an operator where the two components  $\sigma_+$  and  $\sigma_-$  have an additional phase difference of  $\pi$ . It is responsible for the scattering force, essential for cooling atoms. The second term is dominated by the first for large detuning  $\delta$ , and it will then be neglected in the following discussion.

We will now make use of two approximation to simplify the calculations. We first make use of a mean-value approximation for the centre-of-mass degree of freedom. This means that we evaluate the internal states operators appearing in  $d\mathbf{p}/dt$  using the mean position  $\mathbf{r} = \langle \mathbf{r} \rangle + \langle \mathbf{v} \rangle t$ , where  $\mathbf{v}$  is the velocity of the atom. Moreover, since the timescale on which the internal degrees of freedom of the atom evolve are much faster than the timescale associated to the movement of it, we only consider the steady state solution of the atomic dynamics. Making use of the approximations explained above, in the limit  $\delta \gg \Omega, \Gamma$ , where  $\Gamma$  is the decay rate, we find

$$\mathbf{F}_{\text{dip}} = \left\langle \frac{d\mathbf{p}}{dt} \right\rangle = -\frac{\hbar}{2} \frac{\Omega}{\delta} \nabla \Omega \quad (2.7)$$

or, in terms of the potential energy,

$$U = \frac{\hbar}{4} \frac{\Omega^2}{\delta} \quad (2.8)$$

We notice that the dipole force is proportional to the field strength and its gradient, and inversely proportional to the detuning. Moreover, its sign depends on the sign of the detuning. Red-detuned light ( $\delta < 0$ ) generates an attractive potential and can be used to create optical tweezers. This is exploited in our experiment for the creation of the cigar-shaped cloud. On the other hand, blue-detuned light ( $\delta > 0$ ) generates a repulsive potential. This is what we need for the creation of the 2D channel. In the experiment, we use a 660 nm laser, blue-detuned with respect to the Lithium atomic transition of 671 nm.

## 2.2 Spatial light modulation

Now that we know how light interacts with atoms, we are interested in the techniques that can be used to arbitrary shape a light beam. At the basis of these techniques there is Fourier optics, which will be explained in the next section. We will then look at the different tools that can be used to achieve this goal, focusing on the use of phase plates.

### 2.2.1 Fourier optics

Fourier optics is essential to understanding how spatial light modulation works. The basic idea is that a lens returns the Fourier transform of an incident beam on its focal plane. This can be used to transform a phase modulation in an intensity modulation. We will look at this concept in more detail, providing a short introduction to Fourier optics adapted from Saleh and Teich [15] and Schmidt's previous work [14].

Let's suppose we have a monochromatic wave of wavelength  $\lambda$  propagating in the  $z$  direction. In the  $z = 0$  plane, we can denote its complex amplitude with a function  $f(x, y)$ . The function  $f(x, y)$  can be Fourier transformed and decomposed in plane waves propagating in the  $x$  and  $y$  directions

$$f(x, y) = \int d\nu_x d\nu_y F(\nu_x, \nu_y) e^{-2\pi i(\nu_x x + \nu_y y)} \quad (2.9)$$

where  $\nu_x = k_x/2\pi$ ,  $\nu_y = k_y/2\pi$  and

$$F(\nu_x, \nu_y) = \int dx dy f(x, y) e^{2\pi i(\nu_x x + \nu_y y)} \quad (2.10)$$

Each plane wave travels in a direction  $(\theta_x, \theta_y)$ , where  $\theta_i$  is the angle between the direction of propagation and the  $z$  axis on the  $z-i$  plane, and has an amplitude  $F(\nu_x, \nu_y)$ . From Eq. (2.9), we find  $\theta_x = \sin^{-1}(k_x/k) = \sin^{-1}(\lambda\nu_x)$  and  $\theta_y = \sin^{-1}(k_y/k) = \sin^{-1}(\lambda\nu_y)$ .

One way to separate the Fourier components of a wave is by using a lens. A thin spherical lens transforms a plane wave incident on it into a paraboloidal wave focused on a point on the focal plane of the lens (Saleh and Teich Sec. 2.4 [15]). As shown in Fig. 2.1, a plane wave incident at a small angle  $(\theta_x, \theta_y)$  is focused to the point  $(x, y) = (\theta_x f, \theta_y f)$ , where  $f$  is the focal length of the lens. The complex amplitude  $g(x, y)$  at  $z = f$  is therefore proportional to the Fourier transform of  $f(x, y)$  evaluated at  $\nu_x = x/\lambda f$  and  $\nu_y = y/\lambda f$ .

$$g(x, y) \propto F\left(\frac{x}{\lambda f}, \frac{y}{\lambda f}\right) \quad (2.11)$$

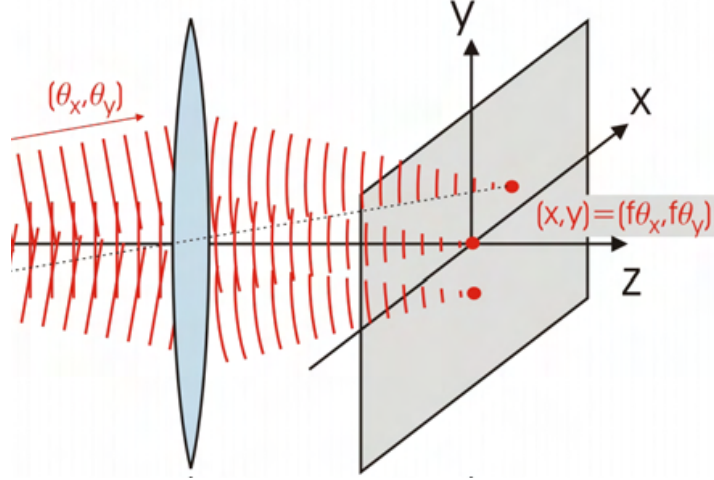


**Figure 2.1:** Focusing of a plane wave into a point. A direction  $(\theta_x, \theta_y)$  is mapped into a point  $(x, y) = (f\theta_x, f\theta_y)$ . The lens is positioned at  $z = 0$  and the focal plane at  $z = f$ . Image from Heine [15]

To find the proportionality factor, we trace the propagation of every plane wave in which we have decomposed the input beam through the optical system. Then we integrate over all these plane waves at the output to obtain  $g(x, y)$ . In the following, we will make use of the Fresnel and paraxial approximations. A field  $F(k_x, k_y)$  can be propagated from the  $z = 0$  plane to the  $z = f$  plane by applying a phase factor  $e^{-ik_z z}$

$$G(k_x, k_y) = F(k_x, k_y) e^{-ik_z z} = H(k_x, k_y, z) F(k_x, k_y) \quad (2.12)$$

with  $k_z = \sqrt{k^2 - k_x^2 - k_y^2}$  and  $H(k_x, k_y, z) = e^{-ik_z z}$ . We can now perform the Fresnel approximation, which states that for plane waves travelling at small angles ( $k_x, k_y \ll k$ ),

$$H(k_x, k_y, z) = e^{-ik_z z} = e^{-iz\sqrt{k^2 - k_x^2 - k_y^2}} \approx e^{-ikz} e^{i\frac{k_x^2 + k_y^2}{2k} z} \quad (2.13)$$

$H$  is defined in the Fourier space, so we can bring it back to the real space applying an inverse Fourier transform

$$h(x, y, z) = \mathcal{F}^{-1}(H(k_x, k_y, z)) = \frac{i}{\lambda z} e^{-ikz} e^{ik\frac{x^2 + y^2}{2z}} \quad (2.14)$$

Now we have to take into account the effect of the lens on the beam. A parabolic lens of focal length  $f$  will apply a phasor  $\phi(x, y) = \exp\left(ik\frac{x^2 + y^2}{2f}\right)$  in addition to the phase acquired by the propagation of the beam. Overall, at  $z = f$ , the field is given by the convolution of the two terms

$$g(x, y) = h(x, y, f) \otimes [\phi(x, y) f(x, y)] = \frac{i}{\lambda f} e^{-ikf} e^{ik\frac{x^2 + y^2}{2f}} F\left(\frac{x}{\lambda f}, \frac{y}{\lambda f}\right) \quad (2.15)$$

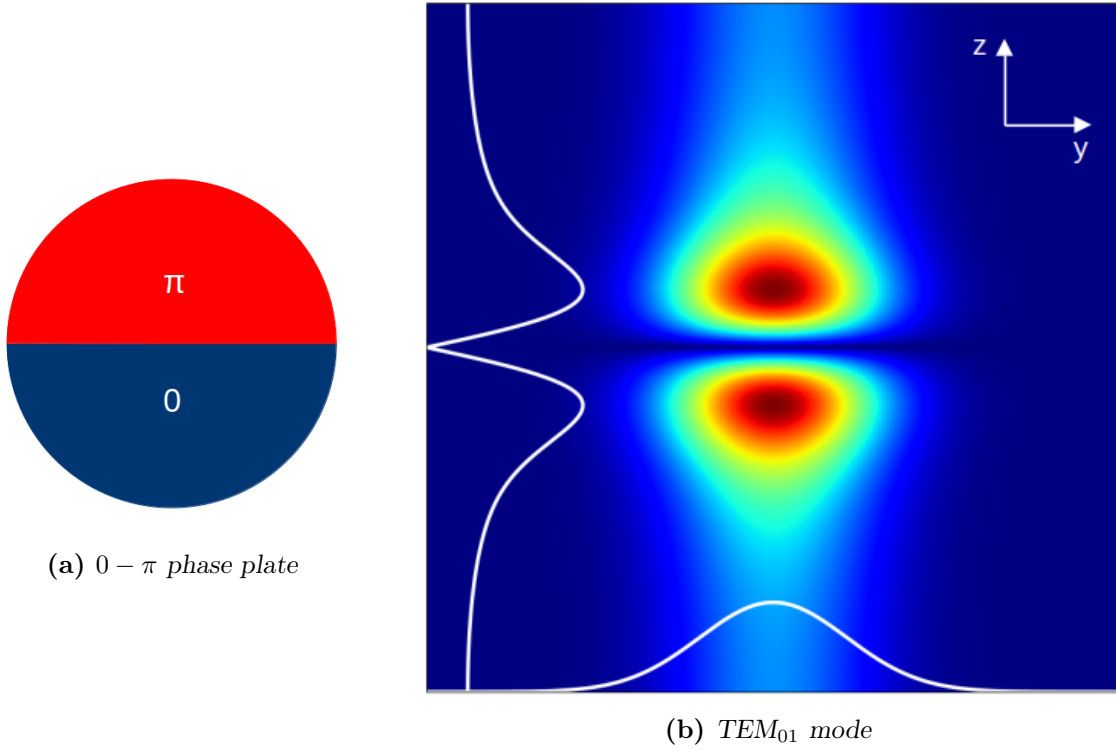


**Figure 2.2:**  $TEM_{01}$  mode generated by a  $0 - \pi$  phase plate. In the figure on the right, the intensity profile at the focal plane is shown together with the integrated intensity along the two axes.

The proportionality factor (up to a phase factor) is therefore found to be  $1/\lambda f$ , and the intensity  $I(x, y)$  at the focal plane is

$$I(x, y) = \frac{1}{(\lambda f)^2} \left| F \left( \frac{x}{\lambda f}, \frac{y}{\lambda f} \right) \right|^2 \quad (2.16)$$

To sum up, a lens returns a Fourier transform of the incident beam at a distance equal to the focal length. This can be used to modulate the intensity profile of the beam.

### 2.2.2 Spatial light modulators: the phase plate

The theory described above can be used as the working principle of numerous devices used for spatial light modulation. Among the ways light can be shaped, it is worth mentioning the use of acousto-optic modulators (AOMs), digital micromirror devices (DMDs), liquid crystals spatial light modulators (LC-SLMs) and phase plates. All these options are good for different purposes. The first three have the advantage of being controllable, allowing the creation of arbitrary shapes simply changing the input signal. The phase plate is cheaper, but once it has been manufactured, it cannot be modified. The use of an LC-SLM for the creation of a uniform light sheet was investigated by Schmidt in his semester project [14]. However, it was found that a phase plate would offer a cheaper and more reliable alternative.

The working principle of a phase plate is very simple. A wave travelling in a transmissive medium has a lower speed than a wave travelling in air. Designing a plate with variable thickness, it is possible to add an arbitrary phase to the beam. The points where the plate is thicker will be delayed with respect to the points where it is thinner. Placing a lens after the plate will result in the desired intensity modulation at the focal plane. One of the simplest example of phase plates is the  $0 - \pi$  phase plate, shown in Fig. 2.2. The plate is divided in two halves, with the upper half out of phase by a factor of  $\pi$  with respect to the lower half. For a beam propagating in the  $x$  direction, the phase profile is then (see Fig. 2.2)

$$\phi(y, z) = \begin{cases} 0 & z < 0 \\ \pi & z > 0 \end{cases} \quad (2.17)$$

This is the phase plate currently used in the experiment, and it generates the  $\text{TEM}_{01}$  mode shown in Fig. 2.2b. As it is clear from Fig. 2.2b, the intensity (and therefore the potential) is not uniform along the  $y$  direction. On the contrary, it has a Gaussian shape, with a peak at the centre. What we would like to achieve is a so-called top-hat potential, shown in Fig. 2.3. It differs from the standard  $0 - \pi$  phase plate in the  $y$  direction. Instead of having a Gaussian profile, it initially ramps up from 0 to 1 (in a.u.), then it remains flat in the central region, and it finally decreases back to 0. In the ramp up region, the profile is Gaussian. In the  $z$  direction, it generates the same kind of intensity modulation as the  $0 - \pi$  phase plate. The region we are interested in is the central region. The phase plate was designed to create an intensity profile as uniform as possible, and this is what we have tried to achieve experimentally.

### 2.2.3 Required specifications

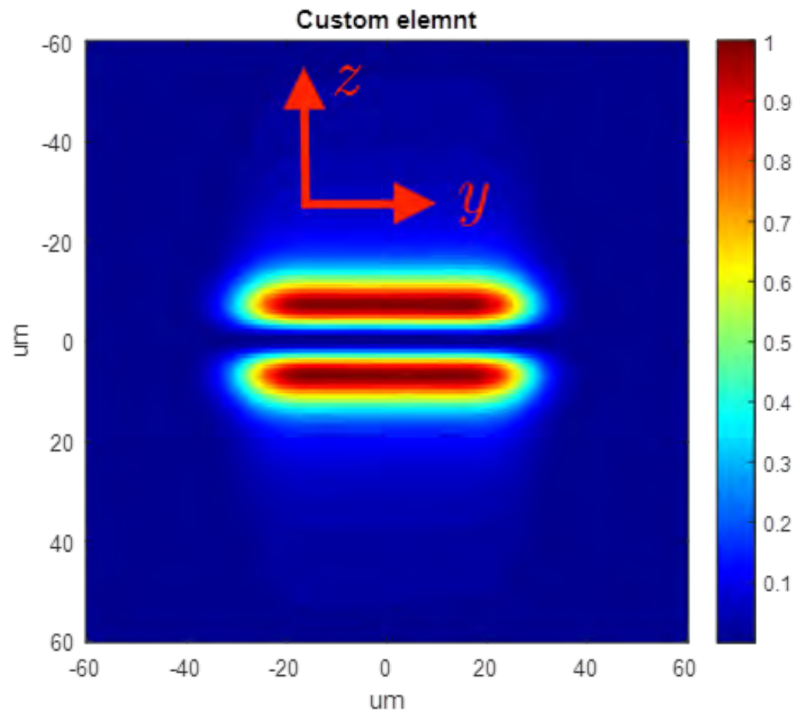
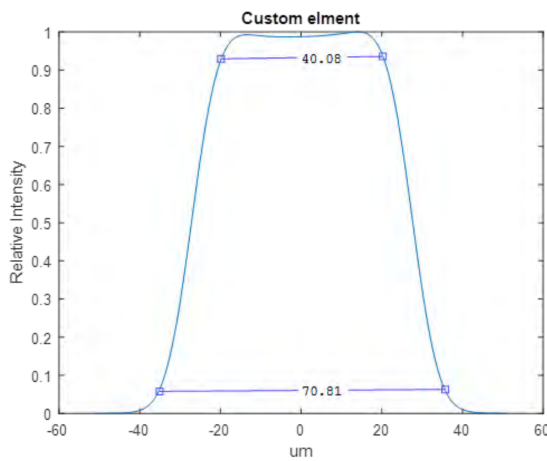
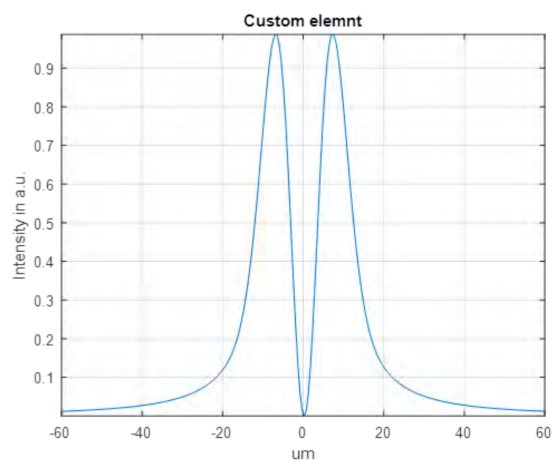
We now turn our attention towards the specifications that the phase plate has to satisfy in order to be useful for our experiment. The three main aspects we want to focus on are the width of the flat region, the darkness  $D$  and the trapping frequency  $\omega_z$ .

The phase plate was designed to create a flat region of  $40 \mu\text{m}$ , with a ramp up region of  $15 \mu\text{m}$ . The specifications are relative to the intensity profile generated by the phase plate in combination with a lens of focal length  $f = 100 \text{ mm}$ . However, in the final experiment it is preferable to use a  $f = 250 \text{ mm}$  lens. Therefore all the features will be scaled up by a factor of 2.5. For example the flat region will be  $100 \mu\text{m}$  long instead of  $40 \mu\text{m}$ .

The darkness is the most important parameter of the phase plate. It gives us a measure of how dark is the dark region at the centre of the light sheet compared to the bright region around. Taking inspiration from Krinner's PhD thesis [13], we define it as

$$D = \frac{I_{\text{node}}}{(I_{\text{max},1} + I_{\text{max},2})/2} \quad (2.18)$$

where  $I_{\text{node}}$  is the intensity at the nodal plane, and  $I_{\text{max},1/2}$  is the intensity at the two maxima. For the experiment to work, the darkness has to be on the 0.1% level. The repulsive laser that creates the 2D channel increases the potential energy with respects to the chemical potential of the reservoirs. If the nodal region is too bright, and therefore the potential energy too high, the atoms will not be able to pass through the channel, and the transport will be suppressed.

(a) *Beam profile*(b) *y direction*(c) *z direction*

**Figure 2.3:** Customized phase plate. In the  $y$  direction, the intensity follows a "top hat" profile, characterized by a Gaussian ramping up, a flat region, and a symmetric ramping down. In the  $z$  direction, the intensity follows the same profile of a  $0 - \pi$  phase plate. The image was provided by Holoor, the manufacturing company.

According to Krinner's work, for a  $0 - \pi$  phase plate and typical powers of 1.3 W, a darkness of one 0.1% increases the potential energy by 70 nK, and the transport is not suppressed.

In order to freeze-out the  $z$  dimension, the trapping frequency must be high enough. If we approximate the trapping potential in the neighbourhood of the nodal plane with a second order polynomial

$$U(z) = U_0 + \frac{1}{2}m\omega_z^2 z^2 + \mathcal{O}(z^4) \quad (2.19)$$

we require the trapping energy  $\hbar\omega_z$  to be higher than the following energy scales [14]:

- Fermi energy  $E_F \approx 600 \text{ nK} = 12.5 \text{ kHz}$
- Binding energy, estimated to be smaller than the 20% of the Fermi energy  $E_B \approx 120 \text{ nK} = 2.5 \text{ kHz}$
- Temperature  $T \approx 60 \text{ nK} = 1.3 \text{ kHz}$

Therefore, the phase plate was ordered to have a trapping frequency of at least  $\omega_z/2\pi = 20 \text{ kHz}$ , much larger than all the other energy scales.

The final goal of using this phase plate is to have a central region as dark and as uniform as possible. The darkness can be evaluated computing  $D$  as explained above in Eq. (2.18). The uniformity of the potential depends on two things: the intensity variation in the central region and the trapping frequency variation. We can understand it by thinking again at the assumption we made for the potential. Assuming that the potential is approximately harmonic, we can write it as

$$U(y, z) = \frac{1}{2}mz^2\omega_z^2(y) + U_0(y) \quad (2.20)$$

where we have explicitly indicated the dependency of  $\omega_z$  and  $U_0$  on  $y$ . Assuming the atoms are in the ground state, they will feel an effective potential dependent on  $y$

$$U(y) = U_0(y) + \frac{1}{2}\hbar\omega_z(y) \quad (2.21)$$

The first term is due to the intensity at the nodal line not being zero. This will add an offset to the potential felt by the atoms. The second term is the energy of the ground state of a harmonic oscillator, where we are assuming again that we can approximate the potential as parabolic in the proximity of the nodal line (see Fig. 2.4). What we want to minimize is then the variation of  $U(y)$  along  $y$ , which will depend both on the variation of  $U_0(y)$  and of  $\omega_z(y)$ .



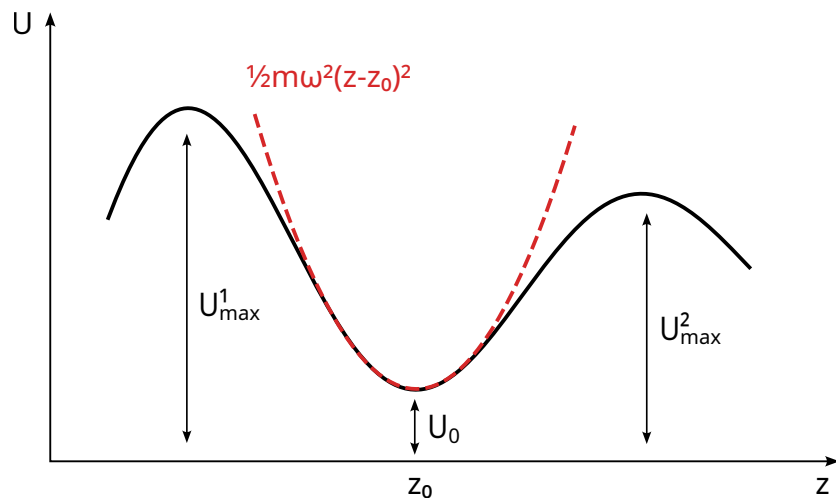


**Figure 2.4:** Potential energy along the  $z$  direction. At the minimum, a non-zero intensity generates a non-zero potential. In the proximity of the minimum the potential can be approximated as harmonic.

## Chapter 3

# Characterization of the phase plate

The final goal of this project was to have a complete characterization of the phase plate that we received from the company Holoor. We knew its expected behaviour, namely the creation of a top hat potential with the characteristics described in Section 2.2.3. However, it was important to test it to see how it behaved in reality. In this chapter, we will discuss the experimental setup and the methods used in the characterization, especially focusing on the quantities we defined to quantify the “goodness” of the result. Then, we will discuss the results highlighting the most important aspects to use the phase plate optimally.

### 3.1 Building the experimental setup

#### 3.1.1 Imaging system

In order to characterize the phase plate, the first step was to set up an imaging system. This was necessary to acquire images of the final intensity distribution. Since the expected dimensions of the intensity distribution were of the order of  $10\ \mu\text{m}$ , a magnification system was assembled. The imaging system was composed of a microscope objective, which magnified the beam, and by a camera. The distance between the two was kept constant by fixing them on a cage. The objective could be moved in the horizontal ( $y$ ) and vertical ( $z$ ) direction by turning two micrometers. The whole system (objective and camera) was mounted on a linear translation stage. The stage could be moved along the  $x$  direction to focus the image. A sketch of the setup is shown in Fig. 3.1.

In order to use the imaging system to take measurements, it had to be calibrated. For the calibration, a laser beam was sent onto a target like the one shown in Fig. 3.2a and imaged. From the image shown in Fig. 3.2b, it was possible to calculate the magnifying power of the imaging system. The lines were measured to be separated by  $413(2)\ \mu\text{m}$  ( $110.1(6)$  pixels of  $3.75\ \mu\text{m}$ ). Knowing that on the target the separation was  $1/55$  mm, we found a magnifying power of  $22.7(1)$ .

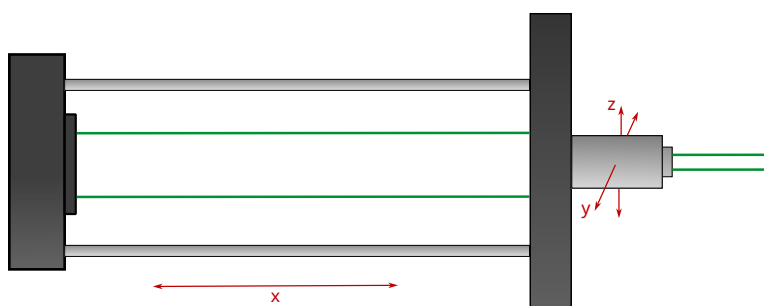
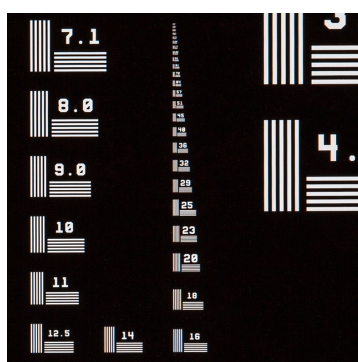
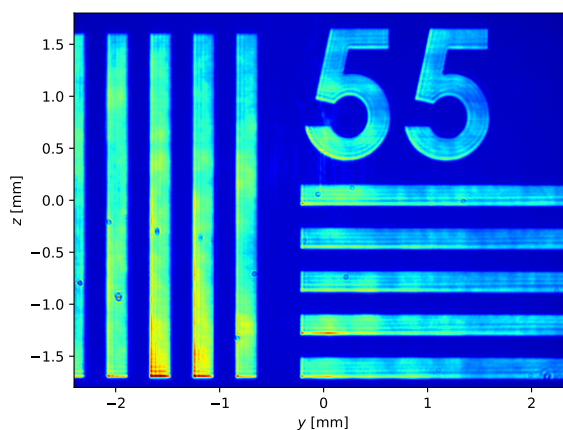


**Figure 3.1:** *Imaging system.* A microscope objective magnifies the image and a CCD camera acquires it. The objective can be moved in the  $y$  and  $z$  direction with two micrometers. The whole system can be moved in the  $x$  direction to focus the image.



(a) Target



(b) Magnified image

**Figure 3.2:** *Calibration of the imaging system.* On the left, an example of a target similar to the one used in the experiment. On the right, the magnified image of a portion of the target. The number 55 means that the target has 55 lines / mm.

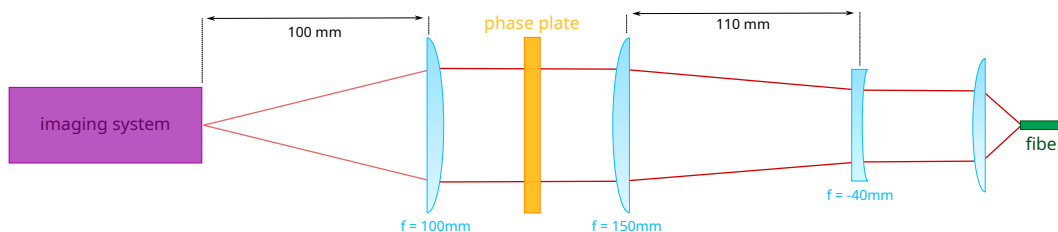


**Figure 3.3:** *Setup for the test of the  $0 - \pi$  phase plate.* The beam coming from the fiber is collimated by a single lens, then expanded by two cylindrical lenses and sent to the phase plate. After the phase plate, an  $f = 100$  mm lens is placed and the result is imaged at the focal plane of the last lens. The two cylindrical lenses and the phase plate are mounted on a rotation mount.

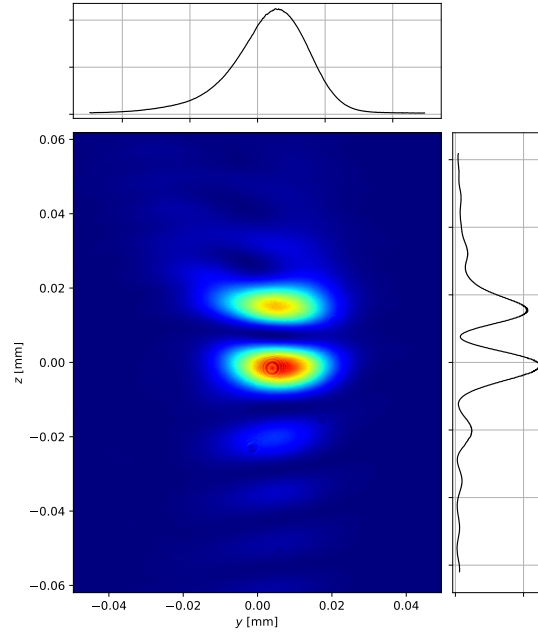


**Figure 3.4:** Intensity distribution after the  $0 - \pi$  phase plate. The size shown on the axis is the real size of the beam. The plots on the right and on top of the image show the integrated sum of the intensity along the respective axes.

### 3.1.2 Test with the $0 - \pi$ phase plate

Before characterizing the top hat phase plate, the setup was tested on the  $0 - \pi$  phase plate similar to the one currently used in the experiment. The laser beam coming from a fiber was collimated with a lens. Then, the beam was expanded in the  $z$  direction by a telescope made of two cylindrical lenses ( $f = -40/150$  mm). The expansion of the beam helped achieve higher trapping frequencies. The beam was then directed to the phase plate and to a  $f = 100$  mm lens. The two cylindrical lenses and the phase plate were mounted on a rotation mount, to allow the alignment of their axis. The result was imaged by the imaging system at the focal plane of the last lens. The focus was adjusted by moving the imaging system along the  $x$  direction. A sketch of this setup is shown in Fig. 3.3.

In order to get good results, it was important that the two cylindrical lenses and the phase plate axes were aligned. To align them, the beam was observed at short and long distances. Acting on the first lens, the beam was rotated in such a way that, when observed at a short distance, its axis was vertical. The same alignment was then performed acting on the second cylindrical lens and looking at the beam at a longer distance. The procedure was repeated, “walking” the beam, until the two lenses were aligned. The collimation of the beam was ensured by using a shear plate. Finally, the phase plate was aligned rotating its axis in such a way that it was parallel to the beam axis.

The final result is shown in Fig. 3.4. The result resembles the expected  $\text{TEM}_{01}$  mode shown in Fig. 2.2b, but it is clear that it could be optimized, making it more symmetric. In particular, the alignment of the whole setup could have been improved. However, since the characterization of the  $0 - \pi$  phase plate was not the goal of the project, the alignment was not refined. Nonetheless, this test was useful to gain familiarity with how phase plates work and with the optics involved in the setup.

### 3.1.3 Shaping the input beam

It had already been reported in Schmidt's work that the most crucial parameter to make the phase plate work is the beam diameter [14]. The phase plate was ordered for a diameter of 6 mm, so this is the first thing we tried to achieve.

#### Single collimating lens + $\times 2$ telescope

Initially we tried to collimate the beam coming from the fiber with a single lens, chosen to produce a 3 mm beam. Expanding the beam with a  $\times 2$  telescope, composed of a  $f = 50$  mm and a  $f = 100$  mm achromatic lenses placed 150 mm apart, we expected a final beam with a diameter of 6 mm. We first tried to collimate the beam with a 15.3 mm C260-TME-A lens (Fig. 3.5a), but the beam was smaller than 3 mm. Then we tried two 18.4 mm lens (Figs. 3.5b and 3.5c). The diameter of the former (C280-TMD-A) was too small ( $\approx 3$  mm, close to the beam diameter), and produced a beam with many aberrations; the latter, with a larger diameter, seemed to solve the problem. The beam was then magnified by the telescope, resulting in the picture shown in Fig. 3.5d.

Given the bad result, we decided to try with a different configuration.

#### Schäfter-Kirchhoff collimator + $\times 3$ telescope

In the second configuration, we collimated the beam with a Schäfter-Kirchhoff collimator (60FC-4-M12-10,  $f = 12$  mm). The collimator was expected to produce a beam with a diameter of  $\approx 2$  mm, which therefore required a  $\times 3$  telescope. The telescope was assembled using a  $-50$  mm lens and a 150 mm lens. Both lenses were achromatic lenses. The use of a concave and a convex lens, beside reducing aberrations, allowed to keep the setup more compact. The beams before and after the telescope are shown in Figs. 3.6a and 3.6b. In Fig. 3.6c it is also shown the profile of the beam after being shaped by the phase plate in combination with a 100 mm lens. It is clear that, despite the general features of the top hat distribution being present, the intensity distribution is very different from the expected one. In particular the top and bottom light sheets seem to be curved around the centre.

#### Single collimating lens

To improve the previous result, we tried to reduce the aberrations using a single achromatic lens to collimate the beam directly to the desired size. In particular, we tried two different lenses: TRH254-040-A-ML ( $f = 40$  mm) and MG 01LAO785 ( $f = 37.5$  mm). The results are

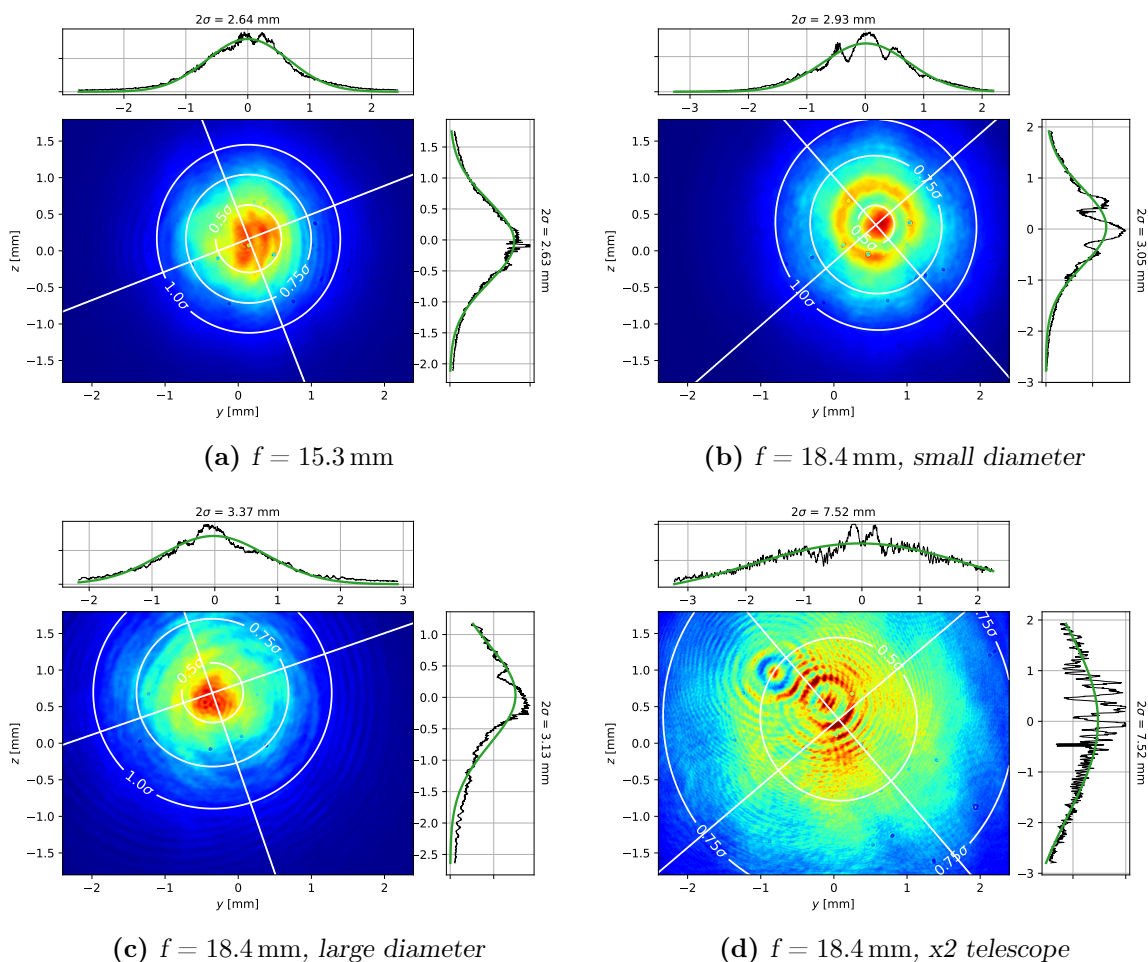


**Figure 3.5:** Beam collimation with a single lens. The focal length of each lens is indicated below the respective figure. In figure (b) and (c) the lenses have the same focal length but different diameter. In figure (d) the beam is magnified with a  $\times 2$  telescope.

shown in Fig. 3.7. Also with this configuration, the result was disappointing, since the beam deviated a lot from the expected Gaussian profile.

### Schäfter-Kirchhoff collimator

Since we were not able to achieve good results only with the optics we had in the lab, we decided to order a collimator with the desired features. In particular, we ordered a Schäfter-Kirchhoff 60FC-L-4-M35-26 collimator ( $f = 35$  mm), specifically designed to collimate large beams. In Fig. 3.8 we show the beam and the result after shaping it with the phase plate and a 100 mm lens. Surprisingly, the result was even worse than the previous ones. Placing the phase plate in the far field with respect to the collimator did not change the result appreciably. Also trying to reduce the aberrations by adding a 1:1 telescope with a pinhole in between did

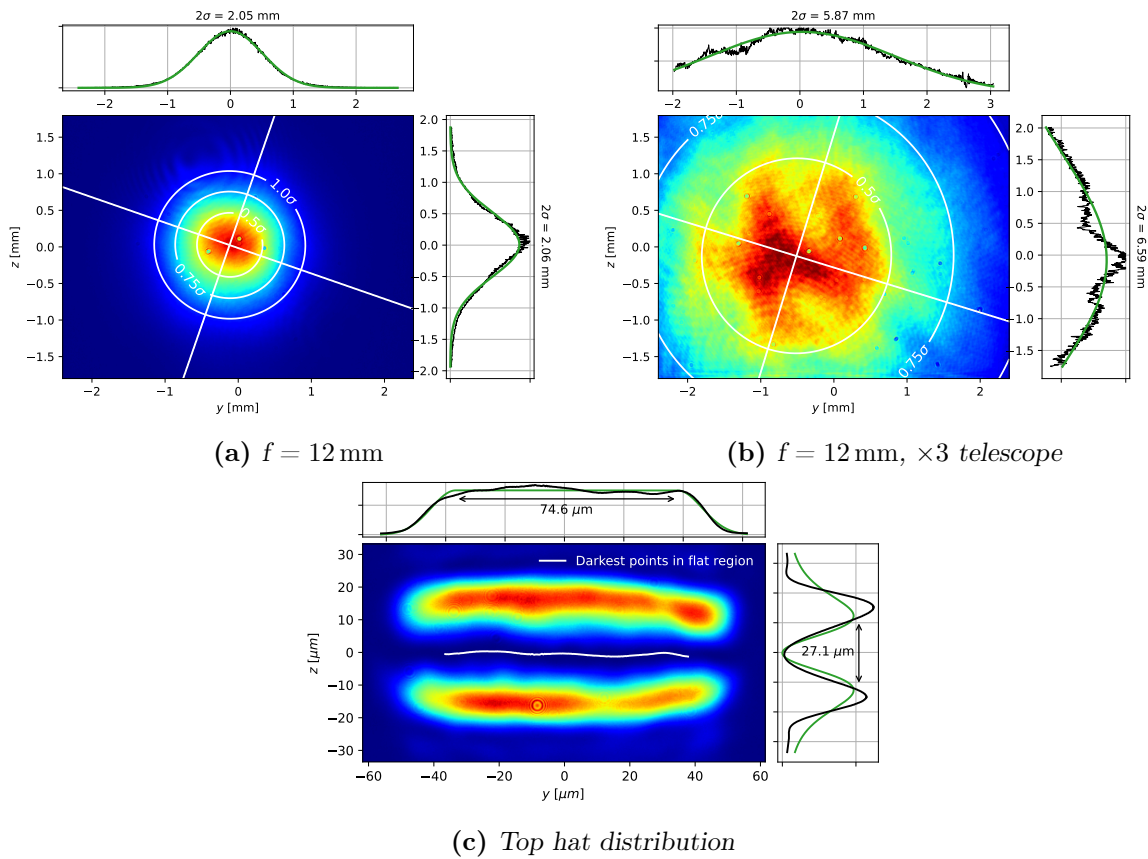


**Figure 3.6:** Beam collimation with a 12 mm Schäfer-Kirchhoff collimator, magnified with a  $\times 3$  telescope ((a) and (b)). The meaning of the fits in (c) are explained Section 3.2.1.

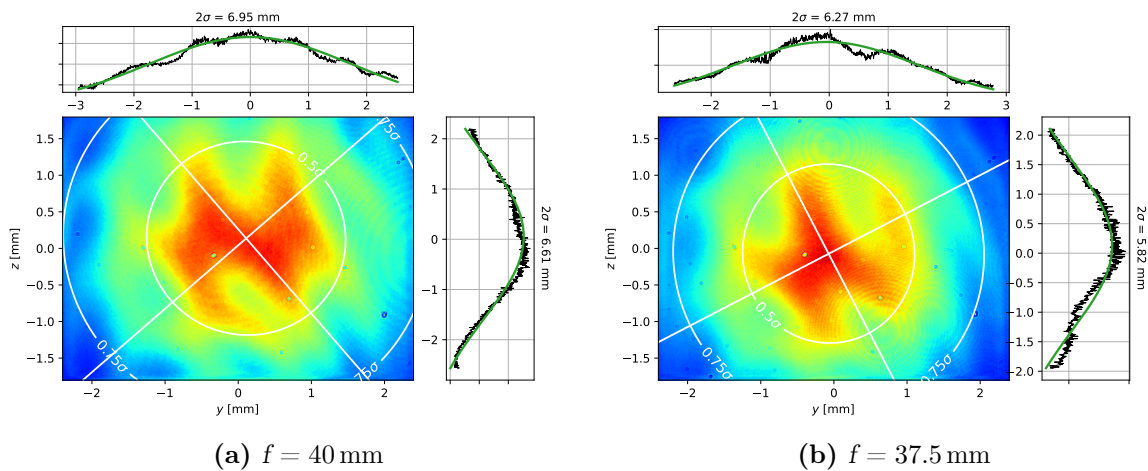


**Figure 3.7:** Beam collimation with a single lens.

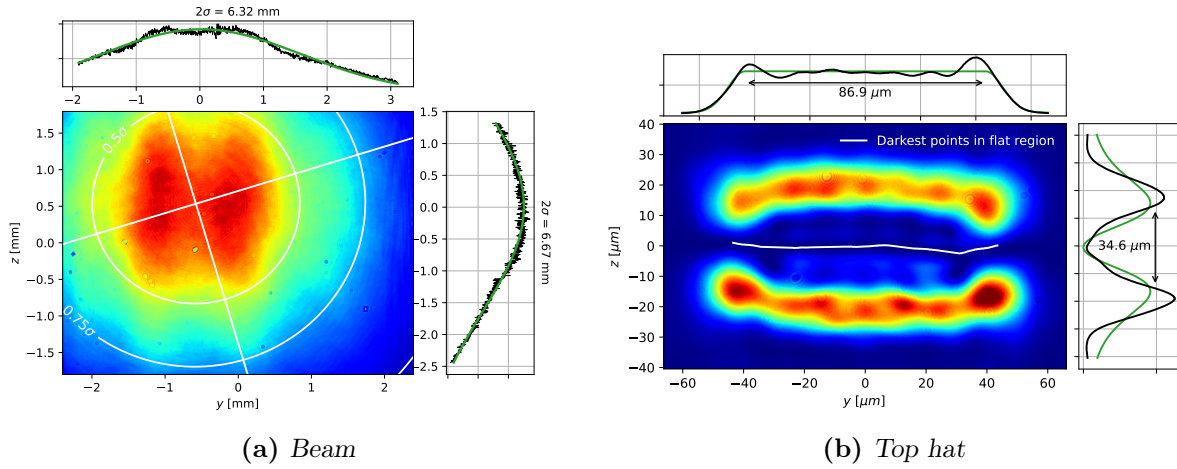


**Figure 3.8:** Beam collimation with a Schäfter-Kirchhoff 35 mm collimator. The first image shows the beam after the collimator. The second image shows the top hat distribution generated by the phase plate together with a 100 mm lens. The meaning of the fits in (b) are explained Section 3.2.1.

not have any noticeable effects.

### Schäfter-Kirchhoff collimator + $\times 3$ telescope with varying beam size

Since even in the (theoretically) best configuration, i.e. using a collimator designed to produce a beam of the desired size, the result was far from optimal, we thought that the problem may have resided in the beam size itself. Therefore, we decided to investigate the influence of the beam diameter on the result more systematically. To do so, we went back to the configuration with the Schäfter-Kirchhoff 12 mm collimator and the  $\times 3$  telescope, with which we had obtained the best result so far (Fig. 3.6). To vary the size of the beam, instead of using the collimator in its usual way, we manually adjusted it to produce a non-collimated beam. A diverging (converging) beam directed to the telescope produced a final beam larger (smaller) than a collimated one. Moving the second lens of the telescope back and forth, it was possible to re-collimate the beam. In this way, we could vary the size of the beam keeping it collimated at the phase plate position. A sketch of this configuration is shown in Fig. 3.9

The results, for three different sizes of the beam, are collected in Fig. 3.10. From the figures, it is clear that the dimension of the beam has a big influence on the result. Even changes of fractions of a millimeter produce great differences in the final result. In particular, it is interesting to observe that for large beams we recognize the behaviour observed in all the previous configurations, i.e. a curvature of the two light sheets around the centre. On the other hand, small beams produce an uneven intensity distribution along the  $y$  axis, with peaks at the border of the flat region. A good compromise seems to be found for a beam of  $\approx 5$  mm. This explains the bad results obtained before, since we were using much larger beams, even if the size was similar to the specifications given by the manufacturer.



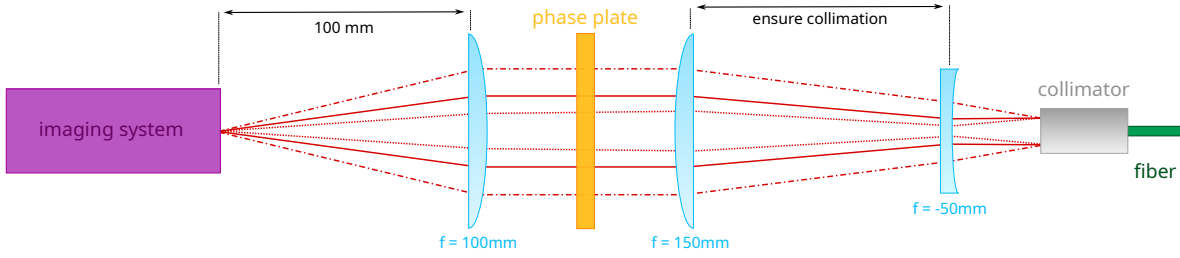


**Figure 3.9:** Setup for the test of the top hat phase plate for various beam sizes. The beam coming from the fiber is (not perfectly) collimated by a Schafter-Kirchhoff collimator, then expanded and collimated by two lenses and sent to the phase plate. After the phase plate, an  $f = 100\text{mm}$  lens is placed and the result is imaged at the focal plane of the last lens.

## 3.2 Characterization

Having found a good beam size which we could aim for, we decided to assemble a telescope that would give us approximately the desired size, and use it to fully characterize the phase plate. For the characterization of the phase plate we decided to keep using the Schafter-Kirchhoff 12 mm collimator, but instead of expanding the beam with a  $\times 3$  telescope, we used a  $\times 2.4$  one. With this setup, we expected a beam with a diameter of  $\approx 4.8\text{mm}$ , size for which we had previously found a good result. The telescope was built with a  $-50\text{mm}$  and a  $120\text{mm}$  achromatic lenses.

For a complete characterization of the phase plate, it was necessary to analyse its behaviour for different beam sizes and different distances from the focus. It was important to look at the light sheet at different distances from the focus because, despite the focal point being in principle well-defined, finding it was non-trivial. Moreover, we did not know if for our goals a non-perfectly focused beam may have been better than a focused one.

### 3.2.1 Methods

Before presenting the results, we offer a brief overview of the methods used to characterize the phase plate. The goal is to define a couple of quantities that can tell us how “good” results are compared to each other, allowing us to find the best possible configuration.

#### Beam characterization

Before diving into the different parameters that were defined to characterize the quality of the light sheet, we briefly mention how the beam itself was characterized. After ensuring the collimation of the beam through the use of a shear plate, a picture of it was taken with a camera. The resulting image was fitted to a 2D Gaussian of the form

$$G(\mathbf{x}) = G_0 + A \exp[-(\mathbf{x} - \mathbf{x}_0)^T \bar{\Sigma} (\mathbf{x} - \mathbf{x}_0)] \quad (3.1)$$

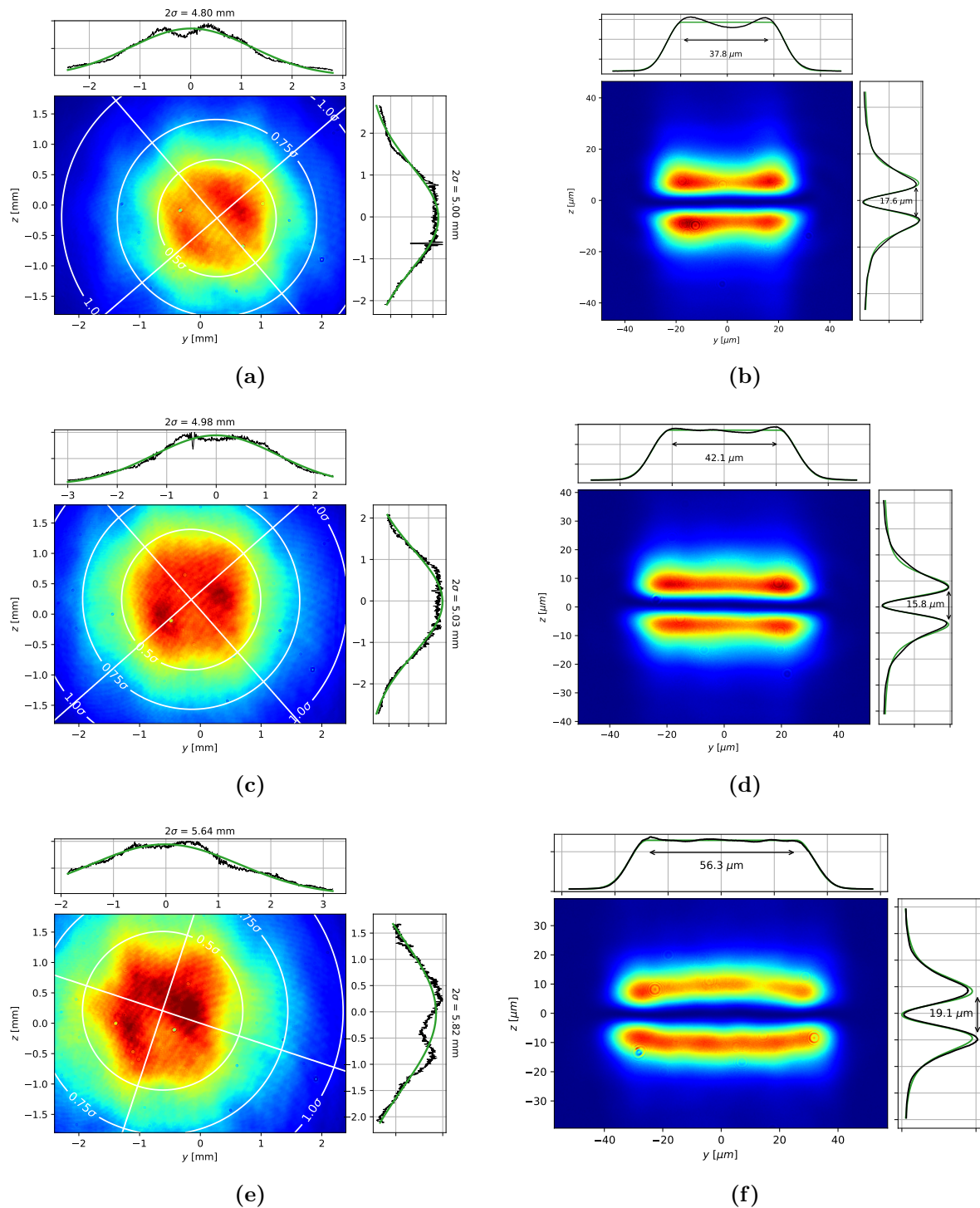


**Figure 3.10:** Beam and top hat distribution for different beam sizes. Every row shows a beam on the left and its respective top hat distribution on the right. The results were obtained with the 12mm collimator and together with the  $\times 3$  telescope. The meaning of the fits on the top hat images are explained Section 3.2.1.

where  $\mathbf{x} = (x, y)$  and  $\mathbf{x}_0 = (x_0, y_0)$  is the centre of the Gaussian distribution. The covariance matrix

$$\Sigma = \begin{pmatrix} 1/2\sigma_x & 0 \\ 0 & 1/2\sigma_y \end{pmatrix} \quad (3.2)$$

was rotated to  $\bar{\Sigma} = R^T \Sigma R$ , where  $R$  is the rotation matrix. For a rotation of an angle  $\theta$ , this would be

$$R = \begin{pmatrix} \cos(\theta) & -\sin(\theta) \\ \sin(\theta) & \cos(\theta) \end{pmatrix} \quad (3.3)$$

The fit is then used to find the size of beam  $\sigma_x$  and  $\sigma_y$  along the two main axes.

### Intensity normalization

For every combination of beam size and distance from the focus, two pictures were taken: a normal (non-saturated) picture and a saturated picture. In both pictures, the background was subtracted by subtracting from each pixel the minimum intensity of the whole picture. The non-saturated picture gave us information on the intensity distribution of the whole light sheet. The saturated picture allowed us to increase the dynamic range of the image in the dark central region, increasing the precision of the measurements. To saturate the picture, we increased the exposure time. Taking note of both the exposure time of the saturated picture and of the non-saturated one, it was possible to “normalize” the saturated picture as

$$I_s^{\text{norm}} = \frac{\tau_{\text{ns}}}{\tau_s} I_s \quad (3.4)$$

where  $\tau_{\text{ns/s}}$  are respectively the exposure time of the non-saturated and saturated pictures,  $I_s$  the intensity measured by the camera for the saturated picture and  $I_s^{\text{norm}}$  the normalized intensity. For both pictures, the absolute intensity  $I_{\text{abs}}$  was found by scaling the intensity measured by the camera  $I_{\text{rel}}$  (already normalized for the saturated image) by a factor given by the power of the laser  $P$  divided by the total power measured by the camera

$$I_{\text{abs}}(y, z) = P \frac{I_{\text{rel}}(y, z)}{\int dy' dz' I_{\text{rel}}(y', z')} \quad (3.5)$$

For all the following calculations, we assumed to have a laser with a power  $P$  of 1 W.

### Global behaviour

The expected intensity distribution generated by the phase plate  $I(y, z) = I_{\text{th}}(y)I_{0\pi}(z)$  is given by a top hat distribution  $I_{\text{th}}(y)$  in the  $y$  direction and by a  $0 - \pi$  distribution  $I_{0\pi}(z)$  in the  $z$  direction. The top hat distribution is defined as

$$I_{\text{th}}(y) \propto \begin{cases} \exp \left[ - \left( \frac{|y| - w_F}{w_R} \right)^2 \right] & |y| > w_F \\ 1 & |y| \leq w_F \end{cases} \quad (3.6)$$

where we have defined  $2w_F$  as the length of the flat region and  $w_R$  as the length of the ramp-up. The  $0 - \pi$  distribution is given by (cf. Krinner's thesis [12])

$$I_{0\pi}(z) \propto \operatorname{erfi}^2 \left[ \frac{z}{w_e} \right] \exp \left[ -2 \left( \frac{z}{w_e} \right)^2 \right] \quad (3.7)$$

where  $\operatorname{erfi}(z) = -i \operatorname{erf}(iz)$  is the imaginary error function and  $w_e$  an appropriate length scale. It is possible to notice that the erfi distribution multiplied by a Gaussian in Eq. (3.7) has two peaks distanced by approximately  $2w_e$ .

Since the two variable  $(y, z)$  of the intensity distribution  $I(y, z)$  are theoretically independent, we can gain some first information looking at the integrated distribution of the intensity along the two axis

$$I_z(y) = \int dz' I(y, z') \quad (3.8)$$

$$I_y(z) = \int dy' I(y', z) \quad (3.9)$$

and fitting the respective distributions  $I_{\text{th}}(y)$  and  $I_{0\pi}(z)$ . This is what was done, for example, in Fig. 3.10d, for which we have found a flat region length  $2w_F$  of  $42.1 \mu\text{m}$  and an erfi distribution with the parameter  $2w_e = 19.1 \mu\text{m}$ .

The integrated intensity  $I_z(y)$  could also be used to calculate a first quantity useful to quantify the ‘‘flatness’’ of the top hat, the so-called peak-to-peak (P2P). The P2P is simply defined as the minimum intensity in the flat region divided by the maximum

$$\text{P2P} = \min_y(I_z(y)) / \max_y(I_z(y)) \quad |y| < w_F \quad (3.10)$$

The closer the P2P is to one, the flatter the top hat distribution is.

### Local behaviour

Even if the previous analysis gives us a good understanding of the global characteristics of the intensity distribution, it fails to be precise about the exact behaviour at the point we are most interested in: the central region. Since the atoms will be trapped in this region, ideally in a 2D space, they will only feel the local potential near  $z = 0$ . It is therefore important to characterize this region with more precision. We have already mentioned in Section 2.2.3 that three important quantities for the characterization of the phase plate are the darkness  $D(y)$ , defined in Eq. (2.18), the trapping frequency  $\omega_z(y)$ , defined in Eq. (2.19), and the effective potential  $U(y)$ , defined in Eq. (2.21). If these three quantities are evaluated for every  $y$ , their mean and their variation will give us information on the darkness of the region, on the strength of the trapping potential and on the uniformity of the potential. To compute these quantities, using the saturated picture, we fitted a parabola in the  $z$  direction for every  $y$ . We then used the fitted coefficients to compute the trapping frequency, the darkness and the effective potential. An example of a fit is shown in Fig. 3.11.

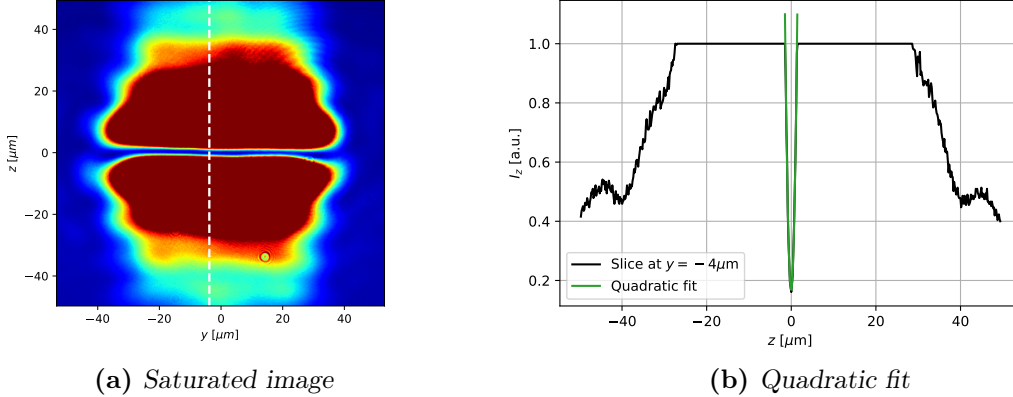


**Figure 3.11:** Example of the quadratic fit of a slice of a saturated image. The slice is taken at  $y = -4 \mu\text{m}$  and it has a width of a single pixel ( $3.75 \mu\text{m}$  on the camera and  $0.17 \mu\text{m}$  before magnification).

### 3.2.2 Results

Pictures were collected for different beam sizes and different distances from the focus. In total, seven beams with diameters between  $\approx 4.8 \text{ mm}$  and  $\approx 5.5 \text{ mm}$  were considered. For every beam size, seven pictures at seven different distances from the focus were taken. Between every picture, the imaging system was moved by  $50 \mu\text{m}$ . We defined the focused image as the one where the peaks found by integrating the intensity along the  $y$  direction were the closest. In practice, after fitting the  $0 - \pi$  distribution  $I_{0\pi}$  to  $I_y(z)$ , we chose the image for which  $w_e$  was minimized (see Eq. (3.7) in Section 3.2.1). An overview of the results is shown in Fig. 3.12.

#### Analysis along the focus

We first present an analysis of the result of the phase plate modulation at different distances from the focus. This analysis shows the behaviour of the phase plate in the  $x$  direction. Below, we discuss the case of the light sheet generated by a beam with a diameter of  $5 \text{ mm}$  (third column in Fig. 3.12). An overview of the results is shown in Fig. 3.13.

First, we computed the characteristic sizes of the light sheets, namely the length of the flat region  $2w_F$  and the distance between the peaks  $2w_e$ . The result is shown in Fig. 3.13a. We notice that the peak distance is minimized for a particular position of the imaging system, which we identified as the focus. On the other hand, the length of the flat region seems to grow linearly while moving along the focus. Then we shifted our attention to the trapping frequency  $\omega_z$  and its relative variation along the  $y$  direction  $\Delta\omega_z/\omega_z$ , where  $\Delta\omega_z$  is the standard deviation of the trapping frequency over different points  $y$ . The trapping frequency  $\omega_z$  was calculated using the overexposed images for higher resolution. The result, shown in Fig. 3.13b, confirms that the focus is well-defined, since at that point  $\omega_z$  is maximal and its variation minimal. We also computed the average darkness  $D$  (Eq. (2.18)), shown in Fig. 3.13d. From the plot, we notice that the darkness increases along the focus. This means that the closer to the phase

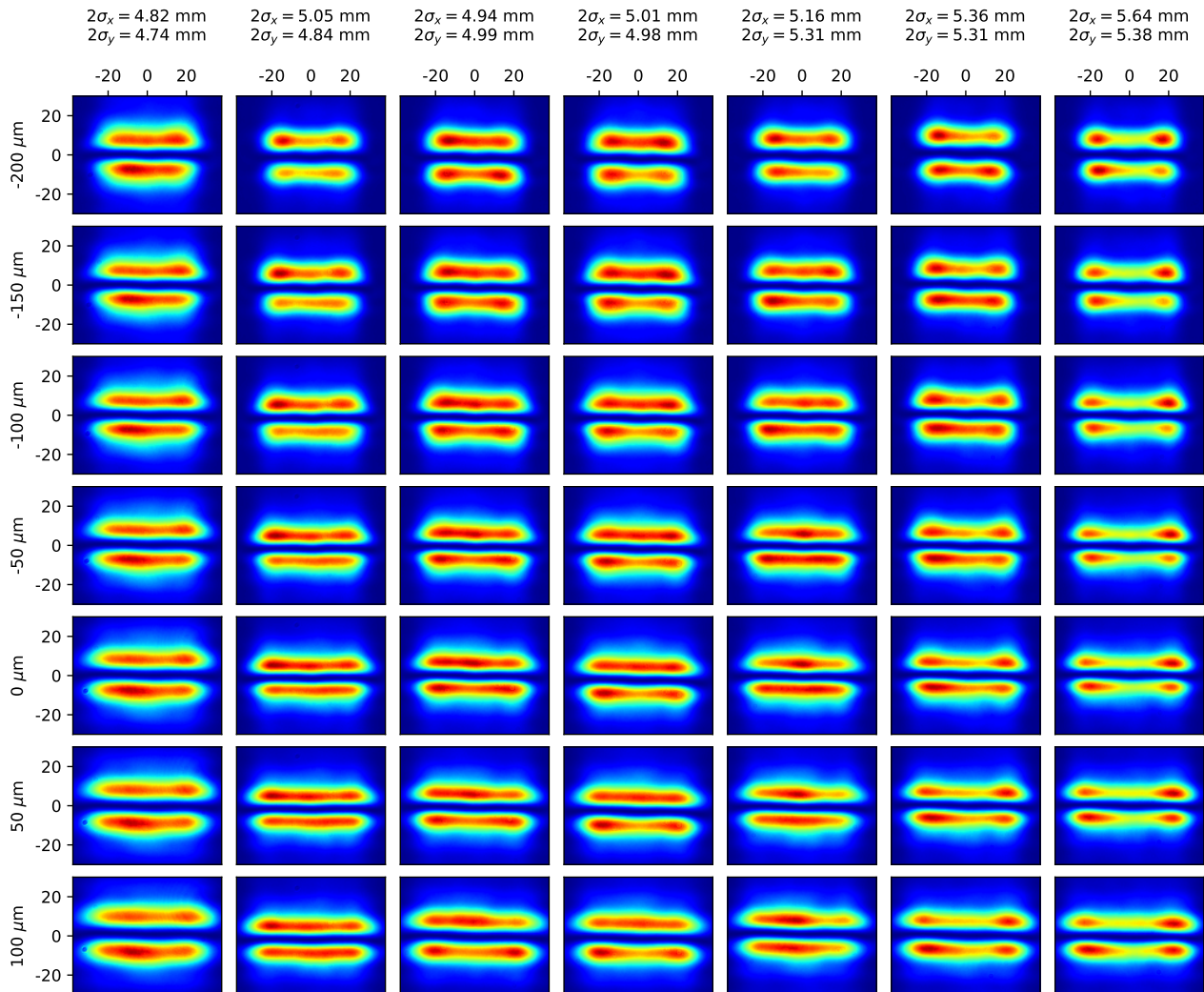


**Figure 3.12:** Overview of the intensity distribution generated by beams of different diameters and at different focal points. The diameter of the beam along its two main axes are shown on top, while the distance from the focus is indicated on the left. Negative distances mean that the image was taken before the focal point, positive distances after. The dimensions of the pictures, shown on the axes, are expressed in micrometers.

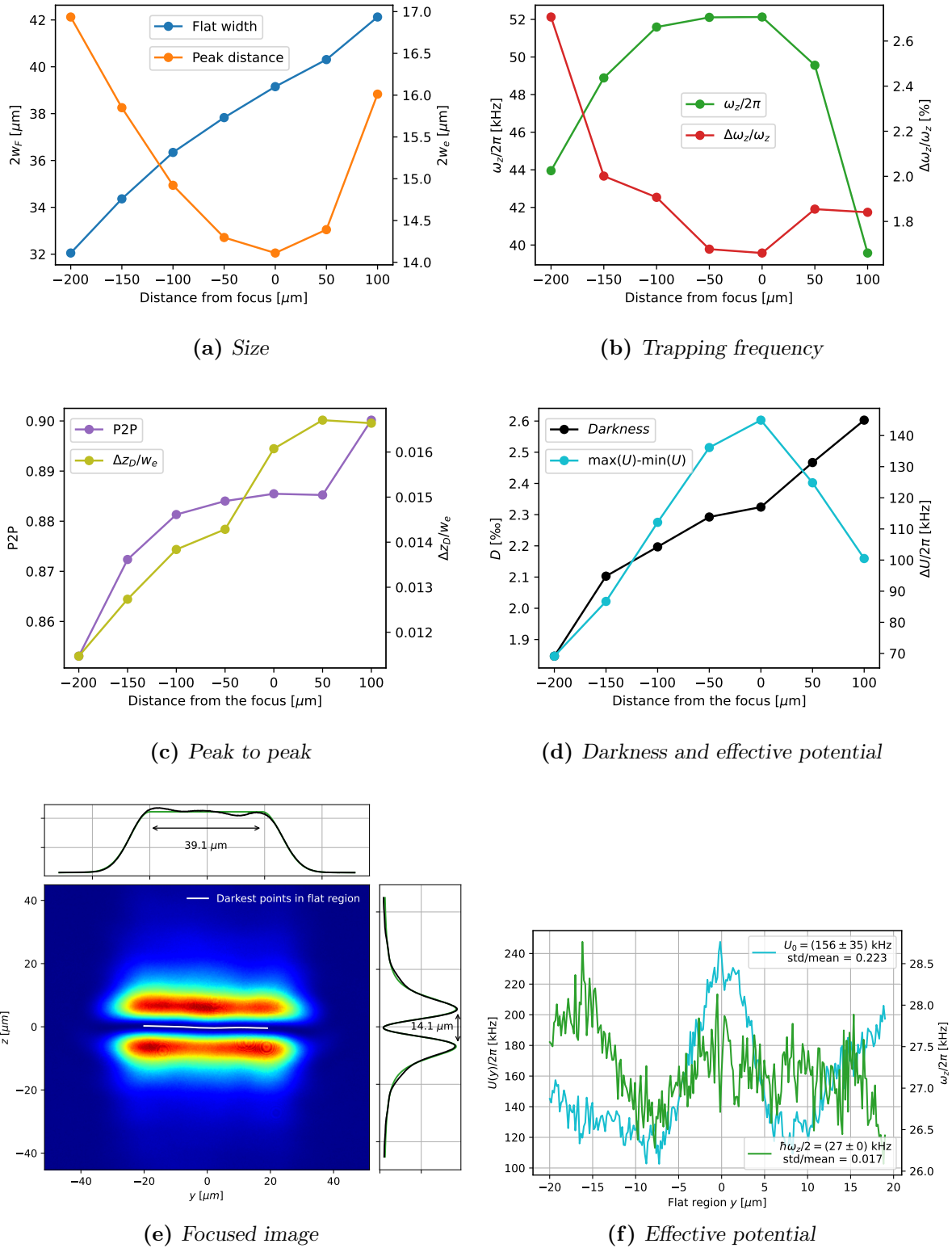


**Figure 3.13:** Analysis of the images across the focus for a beam with a diameter of 5.0 mm. The images (a)-(d) show the dependency of various parameters on the distance from the focus. Picture (e) shows the focused image and picture (f) the variation of the two components of the effective potential along the  $y$  direction for the focused image. Negative distances mean that the image was taken before the focal point, positive distances after.

plate we look, the darker the central region is.

To evaluate the uniformity of the light sheet, we computed three parameters. The first is the P2P, defined before in Eq. (3.10) and plotted in Fig. 3.13c. We notice that it seems to grow, approaching one, while moving away from the focus in the positive direction. This would indicate an intensity distribution that gets more uniform far from the focal point in one direction and less uniform in the opposite direction. Another way to look at the uniformity of the distribution is to look at the position of the darkest point in the central region. These points are shown in Fig. 3.13e as a white line for the focused image. The standard variation  $\Delta z_D$  of their  $z$  coordinate, calculated along the  $y$  direction, is reported in Fig. 3.13c, scaled by  $w_e$ . We notice that the uniformity evaluated in this way has an opposite behaviour compared to the P2P. In fact, the further we move away from the focus in the direction that maximizes the P2P, the more the vertical position of the darkest points varies. This implies that the atoms would not move in a straight line, but they would follow an irregular path. However, if the trap is tight enough and this degree of freedom is frozen, the motion should not matter for the physics of the experiment. The third parameter used to evaluate the uniformity of the light sheet is the difference  $\Delta U$  between the highest and the lowest effective potential felt by the atoms in the flat region along the nodal line, as defined in Eq. (2.21). Surprisingly, this difference has a maximum at the focal point. It is also interesting to notice that it has an order of magnitude of 100 kHz, not negligible compared to the energies involved in our system. An example of the trend of  $U_0(y)$  and  $\omega_z(y)$  along the  $y$  direction for the focused image is also presented in Fig. 3.13f. Here we can notice that most of the non-uniformity of the effective potential  $U = U_0 + \frac{1}{2}\hbar\omega_z$  must be attributed to variations of the intensity on the nodal line, responsible for  $U_0(y)$ . The variation of the trapping frequency  $\omega_z(y)$  is, on the other hand, negligible.

### Analysis of the focused images for different beam sizes

After analysing the behaviour of the phase plate at different distances from the focus, we shifted our attention to the influence of the beam size. For this, we only considered focused images (fifth row of Fig. 3.12). For these images, we computed the same quantities as above. The results are shown in Fig. 3.14.

The characteristic dimensions of the light sheet  $w_F$  and  $w_e$  can be observed in Fig. 3.14a. We notice that the length of the flat region increases with the diameter of the beam, going from a minimum of around 30  $\mu\text{m}$  for a beam of 4.8 mm to a maximum of around 45  $\mu\text{m}$  for a beam of 5.5 mm. This size should be compared with an expected width of 40  $\mu\text{m}$  for a beam of 6 mm. On the other hand, the distance between the two peaks in the  $z$  direction shows an opposite behaviour, decreasing with the increase of the beam diameter.

The behaviour of the trapping frequency, shown in Fig. 3.14b, also shows a clear dependence on the beam diameter. We notice that both its mean value  $\omega_z$  and its relative variation  $\Delta\omega_z/\omega_z$  increase for bigger beams. Moreover, we observe that for all the tested diameters  $\omega_z$  is above  $2\pi \cdot 45$  kHz, therefore enough to trap the atoms in a 2D space. The dependence of the darkness  $D$  (averaged over  $y$ ) is reported in Fig. 3.14d. In this case, we do not observe a clear relation between this parameter and the beam size. For all the beams, we measure a darkness of the order of 4-5 %. This suggests that to optimize the darkness the alignment of the setup is more



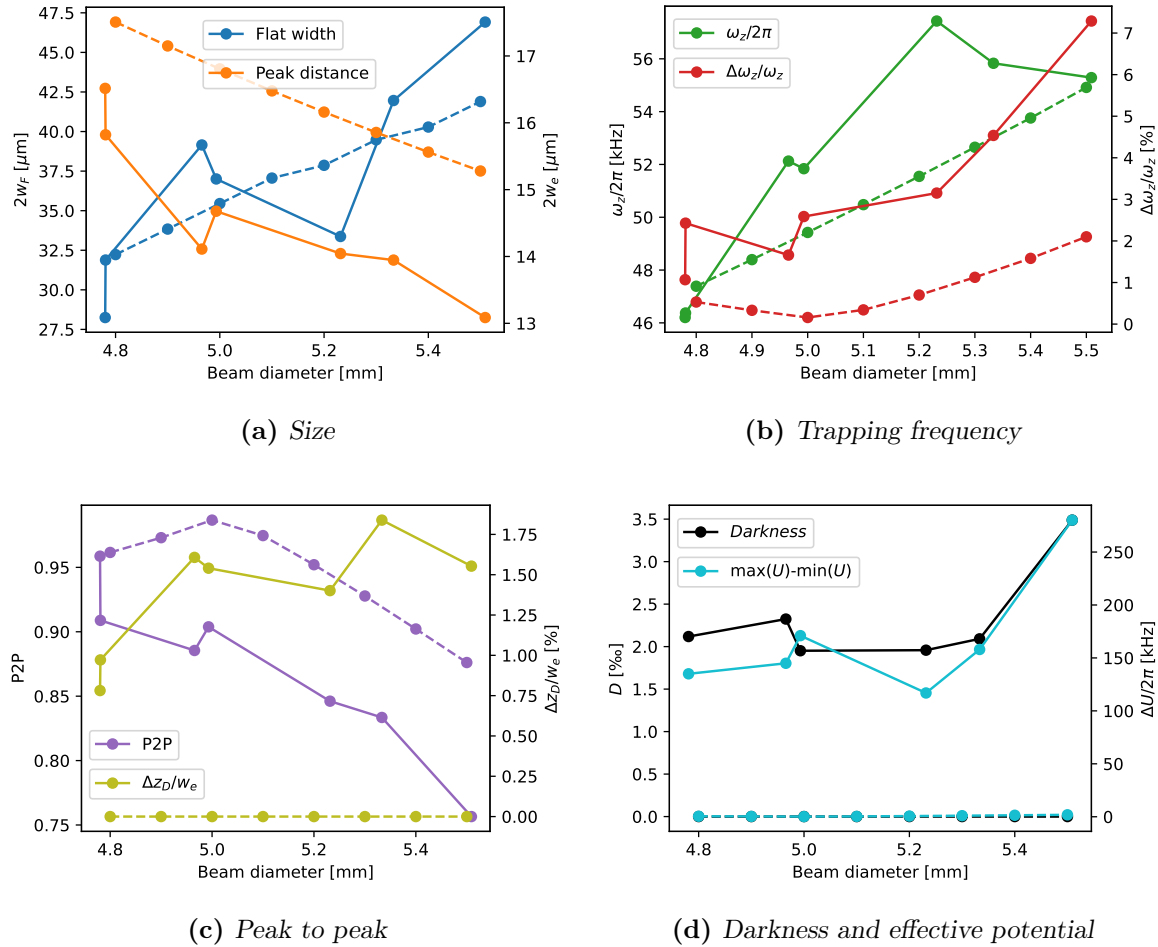


**Figure 3.14:** Analysis of the focused images for different sizes of the input beam. The images (a)-(d) show the dependency of various parameters on the distance from the focus. Picture (e) shows the focused image and picture (f) the variation of the trapping frequency and the effective potential along the  $y$  direction for the focused image. The dashed lines are the result of a simulation with the condition  $2w_f = 37 \mu\text{m}$  and a beam diameter 5.1 mm.

important than the size of the beam.

The uniformity of the light sheet could be evaluated looking at the P2P, at the variation of the position of the darkest points  $\Delta z_D$  and at the difference  $\Delta U$ . The first two parameters clearly show a higher flatness for smaller beams, with a smaller variation  $\Delta z_D/w_e$  and a P2P closer to one. This is also in agreement with what was observed for the trapping frequency, whose variation was smaller for smaller beams. The data for the potential difference  $\Delta U$  is less clear, but still compatible with the same conclusions. In particular, we notice that the potential variation is of the order of 200 kHz (10  $\mu$ K), so not negligible if compared to the energies involved in the system.

In Fig. 3.14 we also report the result of a simulation (dashed lines). To simulate the behaviour of the phase plate, we calculated the phase profile necessary to realize a top hat distribution with a flat region of  $2w_F = 37 \mu\text{m}$  for a beam of 5.1 mm. The beam diameter of 5.1 mm was arbitrarily chosen to have a point at the centre of the experimental data range (between 4.8 and 5.5 mm.) The flat region width  $w_F$  was found through a linear fit of the experimental data. We then used the phase profile to study its effect on Gaussian beams of different diameters. We notice that the behaviour of the typical sizes  $w_F$  and  $w_e$  are consistent with the simulation, even if  $w_e$  is shifted by 10  $\mu\text{m}$ . It is interesting to notice that the measured peak distance  $w_e$  for a beam diameter of 5.0 mm would be consistent with the simulation if the beam had a diameter of 6.0 mm, i.e. the one specified by the company Holoor. This may indicate a mistake in the calibration of the length scale of the camera when measuring the beam size. In the simulation,  $\Delta z_D$ ,  $D$  and  $\Delta U$  are all zero, in agreement with the expectations for a perfectly flat and dark nodal line. The measured trapping frequency  $\omega_z$  is in agreement with the simulation. Its variation  $\Delta\omega_z$  is higher than the simulated one, while the P2P of the experimental data is lower. This is also in agreement with the expectations for a not-perfectly-flat top hat distribution.

### Decreasing the power of the laser

From Fig. 3.14b we notice that in our system we have trapping frequencies of the order of  $2\pi \cdot 50 \text{ kHz}$ . This is actually higher than what we need to confine the atoms in a 2D region. Trapping frequencies of the order of  $2\pi \cdot 20 \text{ kHz}$  would suffice. Therefore, we decided to repeat the analysis for a lower laser power, to see if we could achieve smaller variations in the effective potential  $\Delta U$ , keeping the trapping frequency above  $2\pi \cdot 20 \text{ kHz}$ . In Fig. 3.15 we show the trapping frequency and the effective potential for different beam diameters and a laser power of 0.2 W. We notice that reducing the laser power we can realize light sheets with sufficiently high trapping frequencies and lower variations of the effective potential at the nodal line. In particular, for a laser power of 0.2 W we would keep the trapping frequency above 20 kHz, with a variation of the effective potential of the order of 30 kHz (1.5  $\mu$ K).

### 3.2.3 Additional considerations

Before concluding the report, we present some smaller findings that have proven to be interesting during the characterization process. It may be useful to take them into account when trying to build and align the final setup.

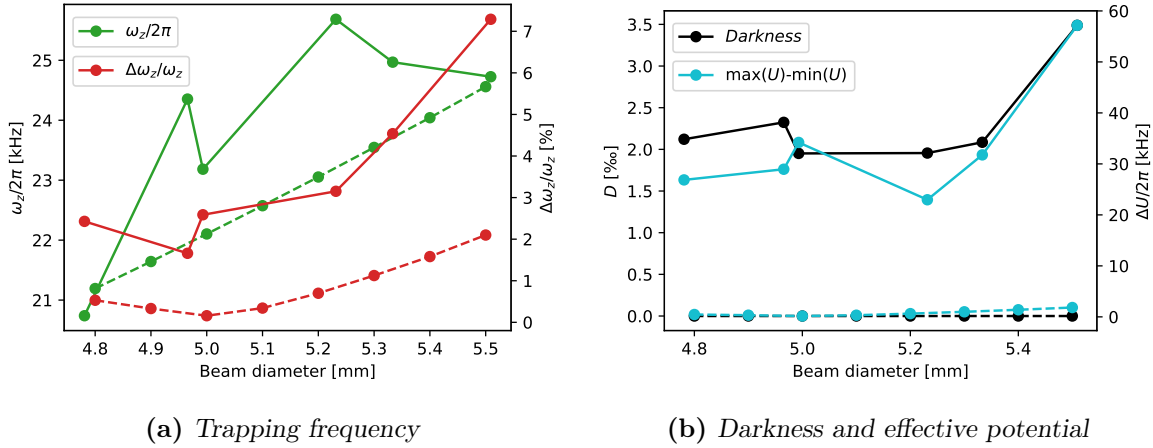


**Figure 3.15:** Trapping frequency, darkness and effective potential for different beam diameters and a laser power of 0.2 W. The trapping frequency is above  $2\pi \cdot 20$  kHz, enough to trap the system in a 2D space, and the variation of the effective potential is of the order of 30 kHz. The dashed lines are the result of a simulation with the condition  $2w_f = 37 \mu\text{m}$  and a beam diameter 5.1 mm.

### Alignment of the phase plate

In order to characterize the phase plate, the setup had to be correctly aligned. The most important alignment procedure was assuring that the beam hit the centre of the phase plate, in particular in the vertical direction. An incorrect alignment resulted in a central region with bright areas, that would suppress the transport of the atoms.

To align the phase plate, the intensity distribution was observed with a camera set with a long exposure time. Most of the pixels of the resulting image were saturated, but not the ones in the central region. Acting on a screw that moves the phase plate vertically, it is possible to optimize the darkness in the central region. An example of aligned and misaligned phase plates is presented in Fig. 3.16.

### Singlet or achromatic focusing lens

It was found that the quality of the focusing lens placed after the phase plate is essential for the final result. In particular, we compared the use of a singlet lens and of an achromatic lens. Both lenses had the same focal length of 100 mm and the beam incident on the phase plate was also the same. The result is displayed in Fig. 3.17. It is clear that the use of an achromatic lens greatly improves the result. The intensity distribution obtained with the achromatic lens is more uniform ( $P2P = 0.86$ ), compared to the one generated by the singlet lens ( $P2P = 0.76$ ).

### Use of a pinhole in the telescope

In order to try to reduce the aberrations introduced by the telescope, the usage of a pinhole placed between the two lenses was investigated for small and large beams. In Fig. 3.18 we

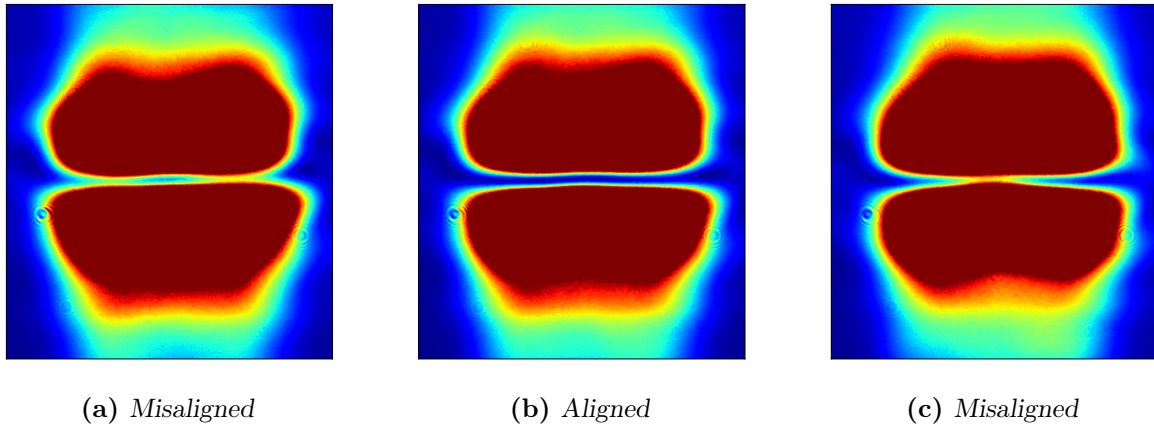


**Figure 3.16:** The vertical alignment of the phase plate is performed looking a saturated picture and optimizing the darkness at the centre.

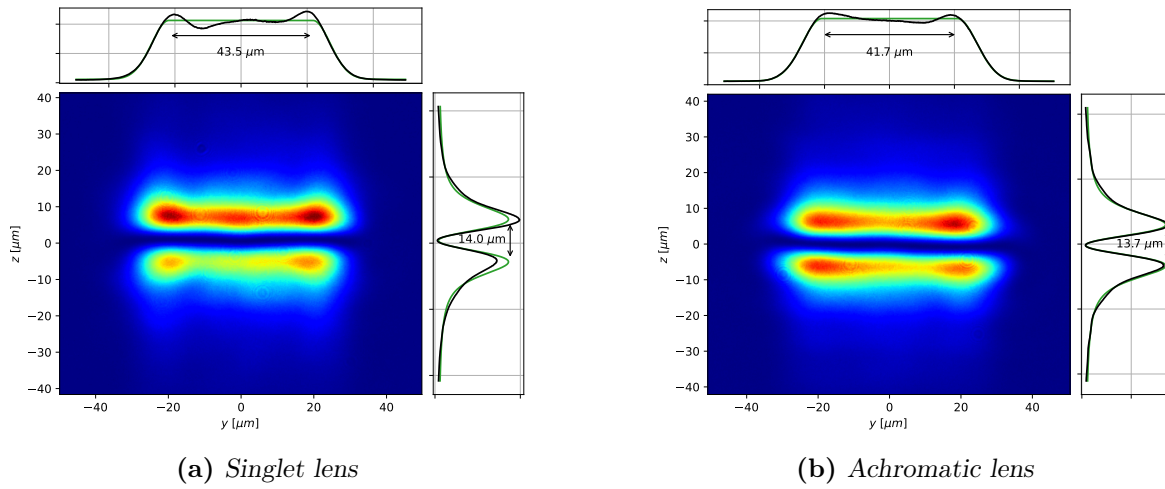


**Figure 3.17:** Intensity distribution for the same beam, but using two different lenses after the phase plate. The first lens (a) is a singlet lens and the second (b) an achromatic lens.

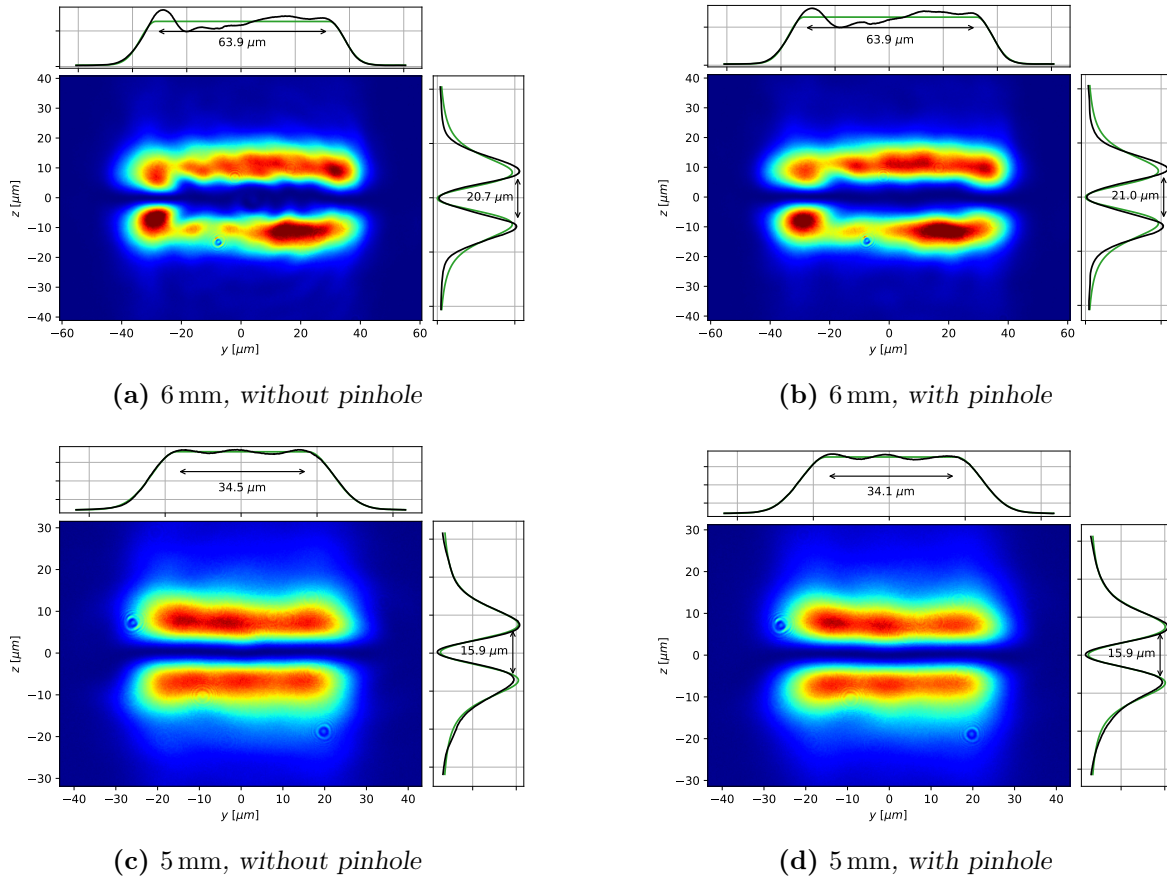
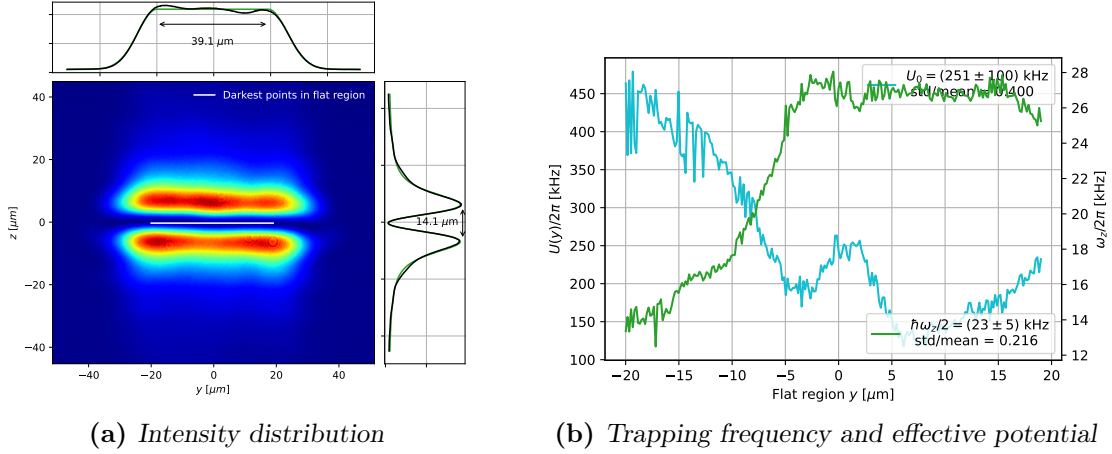


Figure 3.18: Influence of the use of a pinhole in the telescope  $-50/150$  for two beam sizes.



**Figure 3.19:** Analysis of the focused image for a 5 mm beam keeping the coordinate of the position of the dark central region fixed. The result should be compared to Figs. 3.13e and 3.13f.

present the result for the  $-50/150$  telescope. It is important to notice that since the first lens is a diverging lens, the pinhole is almost completely open, and in fact partially “cuts” the beam. However, even in this unusual configuration, the pinhole seems to have an effect. In particular, as it can be observed from the figures, the use of the pinhole reduces spherical aberrations and contributes improving the final result, especially for larger beams. On the other hand, for beams close to the desired size (around 5 mm), it does not seem to have a huge impact on the final intensity distribution.

### Fixing the horizontal dark line

In Section 3.2.1 it was explained how we computed the quantities used to characterize the phase plate. In particular, for quantities like the trapping frequency and the darkness, we fitted a parabola along the  $z$  direction for every point in the  $y$  direction, and extracted the dependency of the parameters on  $y$  (e.g.  $\omega_z(y)$ ,  $D(y)$  ...). For this process, the parabolic function used in the fit had three free parameters, namely the three coefficients of a second order polynomial. This means that the vertex of the parabola was allowed to have an arbitrary height (used to compute the darkness  $D$ ) and position (used to compute  $\Delta z_D$ ).

Another possible approach is to fix the  $z$  position of the vertex  $z_D$ , and fit a function with only two free parameters. In this case, it is logical to set  $z_D$  to the position of the minimum of the integrated intensity  $I_y(z)$ , found by fitting the distribution  $I_{th}(z)$  (cf. Section 3.2.1). The result is shown in Fig. 3.19. We notice that the irregularity of the intensity is moved from a variation in the  $z$  coordinate of the minima to a bigger variation of the trapping frequency and effective potential along the  $y$  direction. In particular, both the trapping frequency and the effective potential show variations larger than a factor of two (between 25 kHz and 50 kHz for  $\omega_z$  and between 12  $\mu$ K and 26  $\mu$ K for  $U$ ). We consider this method inferior to the one described above, since in reality the atoms would move in the region of lower potential, so following an irregular path, rather than in a straight line. The effective potential felt by the

atoms would be the one calculated in the previous section, and not the one found fixing  $z_D$ .

## Chapter 4

# Conclusions

Our tests on the custom-made phase plate have produced interesting and sometimes unexpected results. The central finding of this work is that the parameter to which the shape of the final beam is the most sensible is the incoming beam diameter. In particular, it was found that the optimal beam size is closer to 5 mm than to the 6 mm indicated by the company. Generally, smaller beams produce flatter potentials. At the same time, for smaller beams, the flat region is shorter, such that the potential resembles the TEM<sub>01</sub> which is already being used in the experiment. A trade-off between the two has to be found considering the requirements of the experiment.

In the process of reaching these conclusions, some secondary interesting findings were made. One of them is that the focal point can be found looking at the distance between the two peaks along the  $z$  direction. At the focus, this distance is minimized. We have also found a convenient way to align the phase plate to the centre of the beam, namely looking at an overexposed image and moving the phase plate minimizing the intensity at the nodal plane. Some other secondary findings include the possibility of adding a pinhole in the telescope to reduce aberrations and of using an achromatic lens to focus the beam after the phase plate. Both techniques seem to produce a flatter potential and a lower darkness.

At the end of this project, we were not able to find an optimal configuration that could be used in the final experiment. More tests have to be done to carefully pick the optics most suitable for this use. The information in this report should help assemble a good configuration. Moreover, the influence of aberrations should be better investigated, for example through the use of a Shack-Hartmann sensor.



# Acknowledgements

I want to thank Prof. Tillman Esslinger and Dr. Tobias Donner for giving me the opportunity to work in their group. I would also like to thank Myles and Mohsen for helping me to carry out the project, being always ready to give their valuable contributions and helping me to understand the big picture of what I was doing. Working in this group has been a great experience and I had the possibility to learn a lot.

# Bibliography

- [1] Immanuel Bloch, Jean Dalibard, and Sylvain Nascimbène. “Quantum Simulations with Ultracold Quantum Gases”. In: *Nature Physics* 8.4 (4 Apr. 2012), pp. 267–276. ISSN: 1745-2481. DOI: [10.1038/nphys2259](https://doi.org/10.1038/nphys2259) (cit. on pp. 1, 2).
- [2] Richard P. Feynman. “Simulating Physics with Computers”. In: *International Journal of Theoretical Physics* 21.6 (June 1, 1982), pp. 467–488. ISSN: 1572-9575. DOI: [10.1007/BF02650179](https://doi.org/10.1007/BF02650179) (cit. on p. 1).
- [3] Alexandre Blais et al. “Circuit Quantum Electrodynamics”. In: *Reviews of Modern Physics* 93.2 (May 19, 2021), p. 025005. ISSN: 0034-6861, 1539-0756. DOI: [10.1103/RevModPhys.93.025005](https://doi.org/10.1103/RevModPhys.93.025005) (cit. on p. 2).
- [4] Xiaoling Wu et al. “A Concise Review of Rydberg Atom Based Quantum Computation and Quantum Simulation\*”. In: *Chinese Physics B* 30.2 (Feb. 2021), p. 020305. ISSN: 1674-1056. DOI: [10.1088/1674-1056/abd76f](https://doi.org/10.1088/1674-1056/abd76f) (cit. on p. 2).
- [5] Colin D. Bruzewicz et al. “Trapped-Ion Quantum Computing: Progress and Challenges”. In: *Applied Physics Reviews* 6.2 (May 29, 2019), p. 021314. ISSN: 1931-9401. DOI: [10.1063/1.5088164](https://doi.org/10.1063/1.5088164) (cit. on p. 2).
- [6] Immanuel Bloch, Jean Dalibard, and Wilhelm Zwerger. “Many-Body Physics with Ultracold Gases”. In: *Reviews of Modern Physics* 80.3 (July 18, 2008), pp. 885–964. ISSN: 0034-6861, 1539-0756. DOI: [10.1103/RevModPhys.80.885](https://doi.org/10.1103/RevModPhys.80.885) (cit. on p. 2).
- [7] Felix Bloch. “Über die Quantenmechanik der Elektronen in Kristallgittern”. In: *Zeitschrift für Physik* 52.7 (July 1, 1929), pp. 555–600. ISSN: 0044-3328. DOI: [10.1007/BF01339455](https://doi.org/10.1007/BF01339455) (cit. on p. 2).
- [8] Maxime Ben Dahan et al. “Bloch Oscillations of Atoms in an Optical Potential”. In: *PHYSICAL REVIEW LETTERS* 76.24 (1996) (cit. on p. 2).
- [9] J. Feldmann et al. “Optical Investigation of Bloch Oscillations in a Semiconductor Superlattice”. In: *Physical Review B* 46.11 (Sept. 15, 1992), pp. 7252–7255. DOI: [10.1103/PhysRevB.46.7252](https://doi.org/10.1103/PhysRevB.46.7252) (cit. on p. 2).
- [10] Markus Greiner, Olaf Mandel, and Tilman Esslinger. “Quantum Phase Transition from a Superfluid to a Mott Insulator in a Gas of Ultracold Atoms”. In: 415 (2002) (cit. on p. 2).

- [11] Renate Landig et al. “Quantum Phases from Competing Short- and Long-Range Interactions in an Optical Lattice”. In: *Nature* 532.7600 (7600 Apr. 2016), pp. 476–479. ISSN: 1476-4687. DOI: [10.1038/nature17409](https://doi.org/10.1038/nature17409) (cit. on p. 2).
- [12] Sebastian Krinner et al. “Observation of Quantized Conductance in Neutral Matter”. In: *Nature* 517.7532 (7532 Jan. 2015), pp. 64–67. ISSN: 1476-4687. DOI: [10.1038/nature14049](https://doi.org/10.1038/nature14049) (cit. on pp. 2, 24).
- [13] Sebastian J. Krinner. “Quantum Transport of Ultracold Atoms”. Doctoral Thesis. ETH Zurich, 2015. DOI: [10.3929/ethz-a-010556528](https://doi.org/10.3929/ethz-a-010556528) (cit. on pp. 3, 4, 10).
- [14] Moritz Fontboté Schmidt. “Towards a Uniform Two-Dimensional Channel for Transport Experiments with Ultracold Gases”. ETH Zürich, Feb. 17, 2021 (cit. on pp. 3, 7, 9, 12, 17).
- [15] Bahaa E. A. Saleh and Malvin Carl Teich. “Fourier Optics”. In: *Fundamentals of Photonics*. John Wiley & Sons, Ltd, 1991, pp. 108–156. ISBN: 978-0-471-21374-1. DOI: [10.1002/0471213748.ch4](https://doi.org/10.1002/0471213748.ch4) (cit. on pp. 7, 8).
- [16] Ruth Heine. “Digital In-Line x-Ray Holographic Microscopy with Synchrotron Radiation”. In: (Jan. 2008).



Eidgenössische Technische Hochschule Zürich  
Swiss Federal Institute of Technology Zurich

## Declaration of originality

The signed declaration of originality is a component of every semester paper, Bachelor's thesis, Master's thesis and any other degree paper undertaken during the course of studies, including the respective electronic versions.

Lecturers may also require a declaration of originality for other written papers compiled for their courses.

---

I hereby confirm that I am the sole author of the written work here enclosed and that I have compiled it in my own words. Parts excepted are corrections of form and content by the supervisor.

**Title of work** (in block letters):

Characterization of a phase plate for the creation of an optical homogeneous 2D trapping potential

**Authored by** (in block letters):

*For papers written by groups the names of all authors are required.*

**Name(s):**

Montalti

**First name(s):**

Nicolò

With my signature I confirm that

- I have committed none of the forms of plagiarism described in the '[Citation etiquette](#)' information sheet.
- I have documented all methods, data and processes truthfully.
- I have not manipulated any data.
- I have mentioned all persons who were significant facilitators of the work.

I am aware that the work may be screened electronically for plagiarism.

**Place, date**

Zürich, 18.10.2023

**Signature(s)**

*For papers written by groups the names of all authors are required. Their signatures collectively guarantee the entire content of the written paper.*